FULL RESEARCH ARTICLE



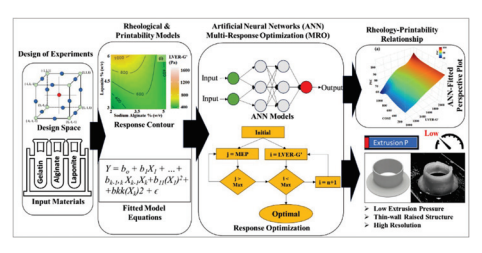
Optimization of printability of bioinks with multi-response optimization (MRO) and artificial neural networks (ANN)

Imtiaz Oavi¹ · Sampa Halder¹ · George Tan¹

Received: 20 February 2024 / Accepted: 28 September 2024 © The Author(s), under exclusive licence to Springer Nature Switzerland AG 2024

In bioprinting, printing resolution and structural stability depend closely on the bioinks' rheological properties such as zero shear viscosity, storage modulus, thixotropic recovery, viscoelasticity, and gelation point. Thus, understanding the material-rheology-printability relationships is crucial for multi-material bioinks. This study adopted a design of experiment (DoE) with response surface methodology using a central composite design to systematically investigate the rheological and print-ability parameters of bio-inks formed through combinations of sodium alginate, gelatin, and a nano-clay reinforcing agent (laponite) for enhanced storage modulus and cellular attachment. The material composition for the optimal printability was determined by the multi-response optimization method. Furthermore, this study incorporated machine learning techniques to generalize the effects of various rheological properties on printability and extrusion pressure. Multi-objective optimization was employed to statistically optimize solution properties based on the two opposing parameters; printed structure conformity and minimum extrusion pressure. The optimized bioinks demonstrated high-fidelity printing performance: less than 5% deformation from the computer-aided-design (CAD) models at low extrusion pressures below 30 Kpa for maintaining good detormation from the computer-aueu-design (CAD) models at low extrusion pressures periow 30 Kpa for maintaining good cell viability. Resampling data from the DoE-fitted model equations facilitated the generation of extensive datasets for train-ing artificial neural network (ANN) models. This process resulted in a robust machine learning model capable of accurately predicting bioink printability with a maximum 6.3% mean absolute error (MAE) solely based on the rheological properties. In summary, the DoE-based data sampling, MRO optimization, and ML modeling approach enabled the development of a robust bioink formulation method applicable to creating bioinks with extreme properties. The study underscores the crucial role of data-driven modelling and optimization approaches in extrusion-based bioprinting for tissue engineering applications.

Graphical Abstract



Extended author information available on the last page of the article

Published online: 08 October 2024



Keywords Bioprinting · Bioink rheology · Response surface modelling · Multi-objective optimization · Artificial neural

1 Introduction

Extrusion-based bioprinting is a well-established 3D bio-fabrication method that involves precise extrusion and layer-by-layer deposition of bio-inks [1–4]. It is renowned for its ability to maintain high cell viability through delicate and controlled ink deposition, allowing for the printing of thick and intricate structures with high cell density, along with a wide range of biomaterial choices [5, 6]. In extrusiona wite range of biolinaterial contest [3]. In Extrusions based bioprinting, achieving an optimized composition of the bioink is crucial to attain the desired characteristics of the printed structures. Furthermore, the extrusion pressure is preferred to be kept below a critical limit to reduce the shear force for cell viability [7, 8]. Altering the material type and the percentage of composition impacts various mechanical and fluidic properties, as well as their biocompatibility, printing pressure, and printability. In our research, we focused on studying and optimizing the rheological char-acteristics of a combination of sodium alginate, gelatin, and laponite to create a bioink with high printability and excellent cellular viability.

Sodium alginate is a widely recognized hydrogel due to its biocompatibility and its ability to form a stable hydrogel structure by reacting with divalent cations like calcium ions [9, 10]. It will maintain long-term structural integrity under various incubation conditions. Gelatin contains cell-adhesive peptides which facilitate cell attachment and proliferation [11–13]. Laponite is a synthetic smectite clay nanomaterial containing layered silicates with magnesium and lithium ions, which can physically and chemically interact with the polymeric matrix of hydrogels [14, 15]. It is used in bio-inks as a rheology modifier to enhance the structural integrity and mechanical support [16, 17]. Our research goal is to develop hybrid bioinks, consisting of these three biomaterials in an optimized formulation, aimed at enhancing printability and structural integrity while maintaining cellular viability.

To achieve this goal, we focused on the interrelationships between bioink composition, rheology, and printability. For bioprinting, rheology heavily influences ink deformation and flow under various conditions, determining printing outcomes such as shape retention and fluid behavior during and after printing [18, 19]. Numerous studies underscore the pivotal role of rheology in bioprinting hydrogels [20–25]. Researchers emphasize its significance as a key physiochemical predictor for high fidelity printing, particularly in extrusion-based bioprinting (20). Paxton et al. identified rheological parameters, including yield stress, shear thinning properties, and power law fit models, as essential criteria for hydrogel-based bioink printability, leading to the development of high-fidelity inks [21]. Townsend et al. stressed the importance of rheology in ensuring high-shape fidelity in 3D bioprinting, highlighting the need for quantifiable standardized methods based on shear performance, recovery time, and yield stress to assess bio-ink printability [22]. Ouyang highlighted the trade-off between cellular viability and printed structure resolution, emphasizing the crucial role of rheology and mechanical behavior in hydrogel-based bio-

In this study, we employed a design of experiment approach to investigate how variations in the concentration of these raw ingredients affect the rheology and printability of the hydrogel structure. We examined key rheologi-cal parameters, including zero-shear viscosity (ZSV), yield stress (YS), shear-thinning index (STI), linear viscoelastic region storage modulus (LVER G'), gelation cross over shear stress (COST), and thixotropic viscosity recovery time (THIX). We employed a central composite design (CCD) to correlate input variables (concentrations of gelatin, laponite, and sodium alginate) with individual rheological and printand solution agriately with individual nicongeral and primi-ability parameters. Surface response plots were generated based on the models developed from the CCD experiment. Furthermore, we applied a desirability function analysis (DFA), a multi-response optimization (MRO) technique, to optimize raw ingredient concentrations for maximum printed structure conformity and viscoelastic properties while mini-mizing extrusion pressure to ensure high cellular viability. Lastly, we utilized an artificial neural Network (ANN)-based machine learning (ML) approach to establish general corre-lations between rheological and printability parameters that are independent of raw material concentrations. Overall, this study established a quantitative correlation, demonstrating ariations in ma terial conc mificantly influ ence both rheological properties and printability parameters

2 Materials and methods

Sodium Alginate (CAS 9005-38-3), derived from brown Sodium Alginate (CAS 9003-38-3), derived from brown algae, was acquired from Sigma-Aldrich (MO, USA) with a standard viscosity range of 4–12 eP in 1% H₂O at 25 °C, Quality level 200. Gelatin (CAS 9000-70-8), sourced from porcine skin and characterized by a gel strength of 300 g



bloom (Type A), was also obtained from Sigma Aldrich (MO, USA). Laponite RD, featuring specifications including a bulk density of 1000 kg/m3 and a pH of 9.8 in a 2% suspension, was procured from BYK (Wesel, Germany). For crosslinking the final structures in the swell ratio test, anhydrous CaCl2 (>96.0%) from J.T. Baker (NJ, USA), which was analyzed and sourced from Avantor (PA, USA), was

2.2 Design of experiments

For the current RSM (Response Surface Methodology) analysis, we employed a central composite design (face-cutered) model to accommodate all response variables acro different concentrations of the materials. The data collected underwent quadratic model fitting, which encompasses main effects, quadratic effects, and interaction effects among the various dependent variables involved in the experiment [26, 27]. In this study, we considered a 3-factor design with high and low levels for the RSM fittings. The total number of experimental samples required was $2^k + 2 k + 1 = 15$ (where k = 15). To assess the robustness of our models derived from RSM fitting, we replicated the central point (start point) three times to calculate experimental error and evaluate the lack of fit. The 15 sets of design points obtained for fitting the RSM model with Laponite (3,6), Gelatin (2,8), and Sodium Alginate (2.5) are presented in the supplementary Table S1

The model equation for the central composite design are as follows [28-30]

$$Y = b_0 + b_1 X_1 + \dots + b_k X_k + b_{12} X_1 X_2 + b_{13} X_1 X_3$$

$$+ \dots + b_{k-1,k} X_{k-1} X_k + b_{11} (X_1)^2$$

$$+ \dots + bkk (X_k)^2 + \epsilon$$
(1)

where h = model intercent

 b_1, b_2, \dots, b_k = co-efficient terms with the main effect terms.

 $b_{12}, b_{23}, \dots, b_{k \cdot l,k}$ = co-efficient terms with the interaction

 $b_{11}, b_{22},, b_{k,k}$ = co-efficient terms with the quadratic effect terms

 $\epsilon = \text{error}.$

The upper and lower bounds of the constituent compositions were determined based on preliminary experimental observations and prior literature. To form physical gel structures. Laponite concentrations of at least 3% (w/v) were deemed necessary [31]. Sodium alginate concentra-tions below 2% (w/v) exhibited low mechanical stiffness and lacked the necessary crosslinked structural stability for hydrogel scaffolds [32, 33]. Previous studies have reported varying starting concentrations of gelatin ranging from 1 to resulting in improved cellular attachment, proliferation and viability [34–37]. Our preliminary experiments indi-cated that endothelial cells exhibited noticeable attachment at a minimum of 2% (w/v) for the commercial gelatin used in our experiment. In earlier literature, alginate concentrain our experiment. In earlier inertaine, agrante coincinnic tions 26% were associated with a significant reduction in cellular viability due to increased viscosity and extrusion pressure (> 35 Kpa). Therefore, for our current experiment, alginate concentrations were fixed between 2 and 5%, striking a balance between the necessary crosslinked strength and optimal rheology for cellular viability. Prior studies on gela-tin-based bioinks have assessed concentrations in the range of 5-10% (w/v) for non-heated extrusion systems, and concentrations above 10% (w/v) were used for heated extruders [38–40]. In line with published literature [41] that explored gelatin-alginate-based bioink extrusion at room temperature, we set our upper limit for gelatin at 8% (w/v). Increasing laponite concentration does add stiffness to the material but can impede polymer flow due to the high laponite matrix density at higher concentrations [42]. Previous research has shown that concentrations of Laponite above 6% (w/v) result in reduced structural height conformity in raised printed structures [43]. Herefore, for our current work, we considered 6% (w/v) as the upper limit for Laponite concentration.

2.3 Rheological measurements

All rheological measurements were conducted using an Anton Parr MCR-92 modular RheoCompass instrument from Austria. Depending on the specific rheological experiments, two types of parallel rotating plates were utilized: (a) 25 mm diameter plates with a 0-degree angle and (b) (a) 25 min diameter plates with a 0-degree angle. For robustness in future investigations, experimental data were collected for three runs to assess the sampling error rate.

2.3.1 Zero shear viscosity (ZSV)

The zero-shear viscosity was determined using a 25 mm parallel plate with a 0-degree inclination in rotary mode. A constant gap of 500 μ m was maintained for all samples to ensure consistent shear force across all experimental runs. Shear rate values were measured in the range of 0.01-1000. with exponentially increasing values at higher shear rates. Initially, the Carreau-Yasuda Model [44, 45] was employed to fit the viscosity data points. Once the model parameters were determined from the fit, the zero-shear viscosity (ZSV) was subsequently calculated using the model equation, as



$$\frac{\eta - \eta_{\infty}}{\eta_o - \eta_{\infty}} = \left[1 + (k\gamma)^a\right]^{\frac{n-1}{a}} \tag{2}$$

where $\eta = \text{viscosity}$ value at any given shear rate (γ)

 η_{∞} = viscosity at infinite shear value. η_{o} = viscosity at zero shear value (ZSV).

= SHEAR rate.

n = power law index.

a = parameter describing the transition from Newtonian plateau to power law region.

Once the model equation has been fitted to the obtained data, the values of k, n, and a are obtained which are then used to determine the ZSV value at the effective zero shear value. Hence, the obtained ZSV value is an extrapolated value where the shear rate is effectively low enough that it replicates the ideal situation mimicking the material at rest.

2.3.2 Shear thinning index (STI)

The shear-thinning property of the prepared bio-inks were assessed using the Ostwald de Waele power-law model [46, 47] which is shown in the following equation:

$$\sigma = K(\gamma)^n$$
(3)

where, σ=shear stress

K = consistency index $\gamma = shear rate.$

n = power-law index

The viscosity data was collected for shear rates rang-ing from 0.01 to 100 mPa.s using a rotary rheometer and 25 mm flat plate. The Ostwald de Waele power-law was fit-ted against the obtained data and the value of the power-law index was tabulated and used as the shear thinning index (STI)

2.3.3 Linear viscoelastic region (LVER) storage modulus (G')

The storage and loss moduli of the bio-inks were deter-The storage and toss modul of the tot-links were determined using oscillatory sweep mode to assess the visco-lastic properties of the prepared bio-ink formulations. All experiments were conducted with a fixed gap of 100 µm, as larger gap values yielded inconsistent results for fluids with low storage modulus. To establish the linear viscoelastic region (LVER) limit, an amplitude sweep experiment was performed. The LVER limit represents the maxi-mum strain rate at which the material exhibits a constant storage modulus (G'). Within the LVER limit, the material undergoes elastic deformation, meaning that upon removal of the shear stress, it returns to its initial form. Beyond the LVER limit, the material experiences permanent deformation and does not recover when the applied shear stress is removed. The amplitude of oscillation was incrementally

increased, varying for different bio-inks since those charincreased, varying to uniferion too-miss since those class acterized as viscoelastic liquids typically exhibited LVER limits at lower shear stresses than bio-inks with solid-like viscoelastic characteristics. During this experiment, G' values were recorded as the maximum storage modulus demonstrated by the bio-inks at their respective LVER

2.3.4 Cross-over (gelation point) shear stress

The gelation point is the specific shear force that triggers a transition in a viscoelastic material from a solid-like state to a liquid-like state. At this juncture, the value of the storage modulus (G') equals that of the loss modulus (G''). Further increase in shear stress beyond this point causes the loss modulus to surpass the storage modulus, leading to a liquid-like flow behavior in the material. The determi-nation of the gelation point, also known as the crossover point, involves the same amplitude sweep experiment used for characterizing the linear viscoelastic region (LVER) limiting G'. In this experiment, we identify the maximum shear stress at which the gelation point occurs (G' = G'').

2.3.5 Thixotropic viscosity recovery

Thixotropic behavior refers to the time-dependent change in the viscosity of structured fluids when they are subjected to shear forces. This property is particularly valuable for characterizing bio-inks because it allows us to replicate the conditions, in terms of changing shear forces, that bio-inks encounter during extrusion printing. All measurements were conducted in rotary mode with a consistent 500 µm agn. A pre-shear value of 10 1/s was applied under isothermal conditions at 25 °C. The experiment consisted of two phases: In the first phase, we obtained five data points at a low shear rate of 0.1 1/s to simulate a resting condition. Data points were collected at a rate of one data point per second. In the second phase, we applied a high shear rate of 100 1/s to replicate the shear forces experienced by biomaintained for one second, with data points collected at a rate of ten data points per second. After this high shear phase, the spindle returned to the low shear rate of 0.1 1/s, and viscosity values were recorded at a rate of two data points per second for a total of 10 min. In this experiment, the recovery rate is defined as the percentage of the initial viscosity that the bio-ink regains within a 5-s timeframe following the high-shear phase. This fixed timeframe was determined based on an assessment of filament spreading due to viscosity breakdown from shear forces in preliminary experiments

2.3.6 Yield stress

In rheology, yield stress is the minimum amount of stress required to initiate the flow in non-Newtonian materials. All the prepared bio-inks are structured fluids, with some showing properties similar to Bingham plastics [48], Below a certain threshold stress, they showed solid-like behavior.
The yield stress is a crucial rheological parameter that correlates to the extrusion pressure requirement for 3D bioprinting applications. For the current project, flow curve measurements were performed at isothermal temperature conditions, with shear rates ranging from 0.01 to 100 1/s. The Herschel-Bulkley model [22, 49, 50] was used to fit the data and determine the yield point. The model equation is shown as follows:

$$\tau = \tau_{HB} + c.\gamma^{p}$$
(4)

where τ = shear stress. τ_{HB} = Herschel Bulkley yield point.

c = flow coefficient. γ= shear rate

p = Herschel Bulkley index.

The value of the Herschel Bulkley yield point was obtained following a model fitting of the obtained data

2.4 Minimum extrusion pressure

The minimum extrusion pressure (MEP) was determined prior to the printing experiments. The extrusion pressure is dependent on the needle and syringes used. Literature survev shows that extrusion needles with diameter < 0.4 mm results in significant reduction in cellular viability induced by cellular stretching and large transition velocity gains [51-53]. The 21G needle with ~0.5 mm internal diamteer is a popular choice in bioprinting applications owing to the match between high cellular viability and printing resolution [54–56] and hence is used in the current work. Furthermore, prior literature shows a linearly proportional relationship between nozzle diameter and extrusion pressure [57]. Hence, based on the appropriate scaling factor, the obtained models can be applied to other nozzle configurations with varying internal diameter and nozzle length. It was the extrusion pressure that resulted in the formation of a 0.98 mm³ ink volume extruded from a 21G needle in 1 s using a near-field camera and image processing. This corresponded to a flowrate volume of 5.88 ml/min of a filament-like material extruded from a 21G nozzle moving at 5 mm/s to form a continuous filament. Since the mixture of the materials show yielding rheological behavior, different extrusion pressure would be required to obtain the same flowrate for different mixtures. The minimum extrusion

pressure in this experiment is defined as the pressure in kPa at which the material starts to flow out from the nozzle. To determine this pressure, we loaded the materials into a 10 mL syringe and allowed them to flow through a 0.5 mm nozzle. The syringe was pressurized with measurable air pressure, and the nozzle tip was observed using a able an pressure, and the nozze try was observed using a microscopic camera system. We collected 10 measurement values for each sample (design points) and recorded both the average and standard deviation values.

2.5 Printing conformity

To assess printing conformity, we measured the dimenis is a seesa priming contorming, we include the time-tance and a contract of the printed structure in comparison to the ideal 3D CAD model. In this experiment, a modified INKREDIBLETM bioprinter (Gothenburg, Sweden) with a fixed nozzle diameter of approximately 0.5 mm was used (Supplementary Figure S1). The printer offers dual extrusion (Supplementary) rigine 31). The printer oriest under extraordinary nozzle attachments with heading capabilities up to 120 °C, translational X–Y accuracies of 10 µm, layer resolution of 100 µm, pressure range of 0–400 Kpa, UV sterilization and curing modes. The flowrate of the bioink is controlled using a pneumatic pump procured from Central Pneumatic (Camarillo, California) operating at 1750 RPM with a maximum delivery pressure of 404 Kpa. The CAD models were sliced using the sli3er (open-source) software and the g-codes and tool path were customized using the Repetier Host (Wil-lich, Germany) software. Various bio-inks were used to print CAD model structures with line widths matching the nozzle diameter, at extrusion pressures slightly higher (around 10%) than their minimum extrusion pressures. We maintained a constant linear transition rate of 10 mm/s and used layer heights of 0.5 mm with a total layer count of 20, resulting in a 1 cm long structure. The layer height was chosen based on experimental trial and error that reduced prior-printed layer penetration by the printing needle for the bioink mixtures that did not strictly follow a filament-like shape. The overall structure was designed to reach a height of 1 cm. After the printing process, we measured the line width and overall height of the uncross-linked structures using ImageJ. We developed a comparative statistic to evaluate how closely the bio-inks adhered to the specified height and width dimen-sions without undesired spreading or collapsing. Structures with low printed structure conformity tended to either collapse under their own weight or spread sideways. The conapse under tien own weight of spirads studentys. In printed structure conformity (PSC) value is essentially an averaged cross-sectional area measurement of the 3D path compared to the modeled cross-sectional area. In our experiment, we collected height and width data from 20 locations (location index) along the printed sample. The printed struc-ture conformity was assessed using the following equation



$$PSC = \frac{\sum_{1}^{i} b_{i} * h_{i}}{B * H}.$$
(5)

where i = location index.

b = measured width. h = measured height

n = number of measu B = modelled width.

H = modelled height

We quantitatively assessed filament stability in various samples using a custom shadowgraph micro-imaging system, examining different temporal and spatial locations. This allowed us to evaluate the stability of the filament from its exit point at the nozzle to specific downstream locations extr point at the indzite to specific downsteam rocations. We also studied how the fluidic properties influenced filament changes at different time intervals within the same spatial locations. The materials were subjected to extrusion pressures approximately 5–10% higher than their mini-mum extrusion pressures. Shadowgraph images of the fila-ments were captured at a frame rate of 8 frames per second (FPS) starting from the moment the liquid began to emerge from the nozzle. We selected three distinct axial position: Y=0 mm (at the nozzle exit), Y=5 mm, and Y=10 mm as spatial measurement points. For assessing temporal stability, we measured the filaments at time intervals of 5, 10, and 15 s.

The equation used to characterize the filament shape/size morphology as an indicator of filament stability for the different design points

$$\frac{\sum_{t=t}^{t=t} \sum_{x=x_1}^{x=x} (N - x_i t_j)}{\sum_{t=t}^{t} \sum_{x=x_1}^{t} (N - x_i t_j)}$$
 (6)

where N = nominal needle inside diameter.

 X_i = spatial diameter. T_j = temporal diameter. X = 0.1, 2, 4 mm.

T = 1, 3, 8 s.

n=total number of data points for all spatial and temporal

2.7 Swelling ratio

The swelling index of a hydrogel material represents its capacity to absorb water or other solvents, typically measured as the ratio of its dry weight to wet weight. In our cur-rent experiment, we prepared samples measuring 2.5 cm in diameter and 1 cm in thickness. These structures were crosslinked in a 2% CaCl2 solution for a total duration of 5 min each. Subsequently, we measured the structures in their wet state. To determine the swelling ratio, we placed then we state: To determine the swering ratio, we practed the samples in a hot oven at 60° C for 12 h before re-measuring their dry weights. The swelling ratio was calculated using the following equation [58, 59]:

$$%S_w = \frac{W_i - W_d}{W_i} * 100$$
(7)

where $S_w =$ swelling ratio

 W_i = wet structure weight W_d= dry structure weight

2.8 Desirability function optimization

To optimize the rheological and printability parameters concerning the concentration of the constituent mixture components, we employed Derringer's desirability function a valuable tool for multi-objective problem optimization This analysis entails converting each response variable into a desirability index (d_i), with values ranging from 0 to 1[60] adestination in the course of the second and the state of the second and the sec demonstrates the relationship between the composite desirability index and the individual desirability index [61]:

$$D = d_1^{w_1} d_2^{w_2} d_3^{w_3} \dots d_{k1}^{w_k}$$
(8)

where, di = Individual Desirability index

 W_k = weight assigned to the individual desirability index D = composite desirability index

The individual desirability indices are then maximized, minimized, or matched to target values using one-sided transformations. The functions for these operations are as follows [62]:

$$d_r^{max} = \begin{cases} 0iff_r(X) < A \\ (\frac{f_r(X) - A}{B - A})^S ifA \le f_r(X) \le B \\ 1iff_r(X) > B \end{cases}$$
(9a)

$$d_r^{min} = \begin{cases} 0iff_r(X) > B \\ (\frac{f_r(X) - B}{A - B})^S ifA \le f_r(X) \le B \\ 1iff_r(X) < A \end{cases}$$
(9b)

$$\begin{split} I_r^{plarget} &= \begin{cases} (\frac{f_r(X) - A}{f_r})^{T_t} i f A \leq f_r(X) \leq t_o \\ (\frac{f_r(X) - B}{f_o})^{T_2} i f f_o \leq f_r(X) \leq B \\ 1otherwise \end{cases} \tag{9c} \end{split}$$

where A = lower acceptable limit.

B= upper acceptable limit

 $t_o = \text{target value}$

s, s1, s2 = desirability satisfaction criteria.

 $f_r(X)$ = the function to be maximized, minimized, or target matched.

The coefficients derived from the RSM models served as the basis for generating objective functions for each rheological and printability parameter. The desirability approach represents a multi-response optimization (MRO) process wherein multiple objective functions are concurrently optimized while adhering to specified constraint limit(s). This optimization process was executed using a scripted program developed in RStudio. The desirability package library in R was utilized to define the composite desirability function based on user-defined individual desirability indices. A penalty approach (rmsOPT), involving the square root of the sum of squares or absolute values of independent variables, was employed to define the optimal input search grid. This grid was designed as either circular or square, depending on the penalty chosen. The search grid was expanded to explore optimal values of the response variables, considering input variables within the experimental ranges. With a search length of 10 per input, this approach resulted in a total of 1000 search combinations for the three materials. An iterative brute-force grid search was conducted to locate the global optimum, and the optimization routine employed was the Nelder-Mead simplex algorithm for convergence.

2.9 Printability assessment of the optimal solution

The optimal solution(s) obtained through the MRO were then assessed using various printability tests based on lifterature [20, 63]. The filament collapse test is a classical filament performance test used to assess the structural integrity of a filament supported at two ends over a distance [63]. A test bed with sequentially incremental gaps of 1, 2, 3, 4, 5, 10, and 20 mm was designed for the collapse test. A schematic of the filament collapse test is available in the supplementary Figure S2. Three different printing speed levels 5, 10, 20 mm/s—were assessed to check the effect of printing speed on filament stability. Images were taken to measure the theoretical area (A_d) to obtain the collapse area factor (C_t) using the following equation [64]:

$$C_f = \frac{(A_t - A_d)}{\Lambda} \times 100\%$$
 (10)

The filament merging and printability index are two popular methods for quantifying the printability of bio-inks. For these tests, grid-shaped structures with 2 mm square-shaped pores were printed, as shown in the supplementary Figure Sa, b. The print path was designed to follow a rectinear propagation of the printing needle, as illustrated in the supplementary Figure S3e, d. Filament merging is a measure

of the amount of material merging-induced deformation at the connection node between two filaments in adjacent layers [20]. Various factors, such as material diffusion and surface tension, influence the amount of filament merging at the nodes [20]. In an ideal case, the diameter of the intermediary filament (R2) would be equal to the diameter of the filament (R1) in the node area. For merging filaments, R2 < R1. The filament merging characteristic is given by the following expression:

Filament Merging =
$$(R2/R1) \times 100\%$$
 (11a)

The filament printability index is a quantitative measure of printability using grid structures defined in prior literature [65]. This is determined using the following formula [65].

$$Pr = \frac{L^2}{164}$$
 (11b)

where Pr, L, and A represent the printability index, perimeter, and the area of the pore region. In ideal cases, the Pr value is equal to 1 [63], resulting in uniform geometric pores. For non-uniform pores formed due to under-gelation of the bioink, the Pr < 1, resulting in pore areas less than the designed model [65]. In grid structures printed from overgelation bioinks, the printability index will be greater than 1 [65]. Since our ideal bioink composition would include gelatin, which exhibits temperature-sensitive flow behavior [66], we tested the ideal bio-ink composition at a fixed printing speed of 15 mm/s, a flow rate of approximately 10% over the minimum extrusion pressure, and varying extruder temperatures (room temperature, 30°C, and 40°C) to assess filament merging and printability index.

2.10 Biocompatibility assessment of the post printed structure

In order to determine the biocompatibility of the prepared bionia, we examined the cellular viability of the optimic composition printed at 10% over its minimum extrusion pressure (-35 Kpa) resulting in a flowrate of approximately 6 ml/ min at an extrusion temperature of 37 °C and printing speed of 5 mm/s. Green fluorescent expressing human umbilical vein endothelial cells (GFP-HUVEC) were purchased from Angio-Protemie (Boston, MA). Cells were cultured in 75 mm² flasks with endothelial growth medium (Angio-Protemie, Boston, MA) supplemented with ampicillin (0.1 mg/ml, Thermo Scientific Chemicals, Waltham, Ma). The original cells were passaged twice before the experiment. The cells were vortexed with bio-ink (2.7 mL) to achieve a final cell density of 0.33 million cells/mL Following the bioprinting process, the cells were stained using Live Dead Viability Kit (AAT Bioquest, Pleasanton, CA, USA) at 37 °C for 30 min. The tive cells were detectable



Progress in Additive Manufacturin

under the green fluorescent protein (GFP) and the dead cells were detectable under the Red Fluorescent Protein (RFP) mode, respectively.

2.11 Machine learning approach for rheological and printability response correlations

In this study, an artificial neural network (ANN) method was employed to establish correlations between rheological parameters and printability parameters. The ANN model was used primarily as a multivariate non-linear regressor tool. Six rheological parameters served as input variables for the ANN, while the outputs consisted of minimum extrusion pressure (MEP) and printed structure conformity (PSC), representing during-process printability parameters. The analysis did not utilize the swelling index ratio trend for different rheological parameters as it is not considered a during-process printability parameter.

during-process printability parameter.

Two distinct neural architectures were developed to predict two different printing parameters. MEP and PSC. These parameters were determined based on the above-mentioned six rheological parameters: ZSV, THIX, COST, YS, STI, and LVER. The initial dataset, consisting of 15 rows of data, was expanded to 1000 row data using iterative resampling through Monte-Carlo simulations. The DOE-fitted function resampling method using Monte-Carlo simulation was shown effective in prior literature for dataset expansions [63–70]. To assess the printability parameters beyond the input variable range, synthetic data points were generated using a generative adversarial network (GAN) architecture, resulting in an additional 1000 rows of data. The GAN-generated data was validated using the original 15 DOE design points which were used as the test set for evaluating the data accuracy. For both models, the Keras Sequential and TensorFlow packages within R were employed. The specific architectures of both models were generated using a trial-and-error approach to determine the optimal number of layers that would minimize the mean squared error (MSE) for each model.

Initially, we started with a single hidden layer containing six neurons and progressively added subsequent layers with the same number of neurons. For the PSC data, we found that adding three hidden layers would yield the lowest MSE, while for the MEP data, two hidden layers resulted in the lowest MSE. However, for more than three hidden layers, data overfitting occurred for both MEP and PSC, as evidenced by the validation error surpassing the training error after 50 epochs. This indicates that the model tended to shift towards low-bias and high-variance models with higher layers [71]. Hence, the chosen number of layers provided a suitable model complexity that struck the optimal bias-variance trade-off [72]. After determining the number of hidden layers for each model, we conducted hyperparameter tuning

using the Keras Tuner [73]. This involved optimizing the number of neurons in each layer within specified ranges, ranging from 2 (23 of input neurons) to 32 (533 times the input neurons) for each layer. The goal was to minimize both the training and validation errors over 100 epochs. A Random Search Keras tuner algorithm [74] with three executions per trial was performed to match the objective of minimizing training/validation error. The models with the lowest training and validation errors are depicted in Figure 3.

The first phase of testing involved one-fold cross-validation. The dataset from Multi-Response Optimization (MRO) was split into a 80:20 ratio for training and testing sets of the neural network models for both MEP and PSC. A validation split of 20% was applied to the training dataset. Subsequently, the models were tested again using k = 5 for k-fold cross-validation, and the average mean squared error (MSE) and mean absolute error (MAE) were found to be similar to those obtained in the single-fold cross-validation. To normalize the dataset, a standard scaler was applied.

The PSC model featured three hidden layers with four hyperbolic tangent (TanH) activation neurons, four rectified linear unit (ReLU) neurons, and three leaky-ReLU neurons in the respective layers. Additionally, it employed an L1 regularization scheme with a regularization factor of 0.001 and a layer dropout rate of 0.1 to prevent overfitting. The output layer consisted of one neuron with a linear activation function suitable for numerical model fitting.

On the other hand, the MEP model employed two hid-

On the other hand, the MEP model employed two hidden layers with four TanH and four ReLU neurons in the
subsequent hidden layers. It incorporated L1 regularization
with a factor of 0.01, a layer dropout rate of 0.5 in the first
layer, and a layer dropout rate of 0.1 in the second layer
to prevent overfitting. The TanH function squashes input
values into a range between –1 and 1, while ReLU converts
values to a range between of and 1, setting values less than 0
to 0. To address the 'dying ReLU' problem caused by negative values being set to 0, the leaky ReLU was used, which
introduced a small bias (e) to prevent 0 values for negative
inputs. The functional form of the TanH, ReLU and Leaky
ReLU activation functions [75–78] are as follows:

TanH:
$$g(x) = \frac{e^x - e^{-x}}{e^x + e^{-x}}$$
 (12a)

$$ReLU : g(x) = max(0, x)$$
 (12b)

Leaky ReLU:
$$g(x) = \max(\epsilon x, x)$$
 with $\epsilon << 1$ (12c)

Both the models were compiled with loss definitions set to mean square error (MSE). The Adam optimizer with learning rates of 0.005 was used to update the weights of the neural network. The Adam optimizer was chosen owing to its advantages of momentum and adaptive learning rates.

The neural network shapes for predicting the PSC and MEP

3 Results and discussion

3.1 Model equations and response surface from the CCD-RSM method

Following the data obtained from the experimental procedures based on the design of experiment table, the model coefficients are obtained by regression fitting to the model Eq. 1 which contains the Main effects, and the significant interaction, and quadratic effects. The model fitting was performed using the RSM package in RStudio which is an extension of the linear model (lm) function in base R [79]. For better elucidation of the intercept and the unit change of response for unit change in factor, a scale-invariant method is implied by coding the factor estimates. The following model equations provide the estimates (P<0.1) using coded factor levels (half-effects):

$$\begin{split} \textbf{ZSV} &= 10.64 + 21.76(\textbf{X}_1) + 7.12(\textbf{X}_2) - 4.55(\textbf{X}_3) \\ &+ 14.74(\textbf{X}_1)^2 + 7.57(\textbf{X}_3)^2 + 16.52(\textbf{X}_1.\textbf{X}_2) \\ &- 17.47(\textbf{X}_1.\textbf{X}_3) - 5.33(\textbf{X}_2.\textbf{X}_3) \\ &[\textit{Model RSq} = 0.96] \left(\text{Unit: } \times 10^4 \text{mPa.S} \right) \end{split} \tag{13a}$$

$$\begin{split} \mathbf{STI} &= 0.57 - 0.06(\mathbf{X}_1) - 0.1(\mathbf{X}_2) + 0.128(\mathbf{X}_3) \\ &- 0.16 \big(\mathbf{X}_1\big)^2 - 0.06(\mathbf{X}_1.\mathbf{X}_3) [Model \, RSq = 0.81] \end{split} \tag{13b}$$

$$\begin{split} \textbf{LVER-G'} &= 636.33 + 210(\textbf{X}_1) - 94.1(\textbf{X}_2) \\ &+ 193.6(\textbf{X}_3) + 372.27(\textbf{X}_1)^2 \\ &- 247.88(\textbf{X}_2.\textbf{X}_3)[Model\,RSq = 0.83] \end{split} \tag{13c}$$

THIX =
$$0.72 - 0.06(\mathbf{X}_1) - 0.14(\mathbf{X}_2)$$

+ $0.03(\mathbf{X}_3) + 0.09(\mathbf{X}_1)^2 - 0.14(\mathbf{X}_2, \mathbf{X}_3)$ (13d)
- $0.09(\mathbf{X}_1, \mathbf{X}_3)[Model RSq = 0.82]$

COST =
$$33.82 + 283.56(\mathbf{X}_1) + 42.02(\mathbf{X}_2)$$

 $-137.68(\mathbf{X}_3) + 266.75(\mathbf{X}_1)^2$ (13e)
 $-309.68(\mathbf{X}_1.\mathbf{X}_3)[Model RSq = 0.90]$

Swelling Ratio =
$$28.48-2.60(\mathbf{X}_1)-5.60(\mathbf{X}_2)-7.08(\mathbf{X}_3)$$

+ $8.85(\mathbf{X}_3)^2 + 2.81(\mathbf{X}_1.\mathbf{X}_2)$
[Model RSq = 0.90]

$$\begin{aligned} \textbf{Yield Stress} &= 17.61 + 17.52(\textbf{X}_1) - 9.67(\textbf{X}_2) \\ &- 6.53(\textbf{X}_3) + 12.13(\textbf{X}_1)^2 - 8.22(\textbf{X}_2)^2 \\ &+ 14.89(\textbf{X}_3)^2 - 29.61(\textbf{X}_1,\textbf{X}_3) \\ & [\textit{Model RSq} = 0.82] \end{aligned} \tag{13g}$$

Printing Conformity =
$$16.14 + 26.62(\mathbf{X}_1) - 11.72(\mathbf{X}_2)$$

+ $5.50(\mathbf{X}_3) + 27.78(\mathbf{X}_1)^2 - 12.5(\mathbf{X}_1 \cdot \mathbf{X}_3)$
- $8.19(\mathbf{X}_2 \cdot \mathbf{X}_3)[Model RSq = 0.85]$
(13h)

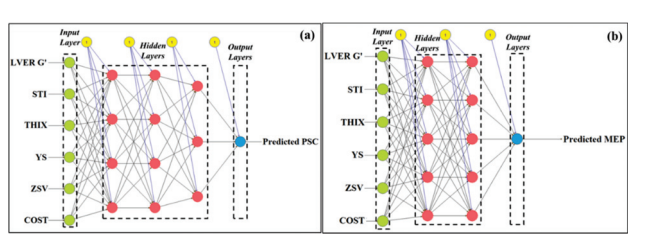


Fig. 1 The neural network architectures used to model the relationship between the rheological parameters and a PSC b MEP

$$\begin{aligned} & \text{Minimum Extrusion Pressure} = 14.58 + 18.92(\mathbf{X}_1) \\ & -4.97(\mathbf{X}_2) - 5.12(\mathbf{X}_2) + 13.69{\left(\mathbf{X}_1\right)}^2 \\ & -14.65(\mathbf{X}_1\mathbf{X}_2) \left[Model\,RSq = 0.91 \right] \\ & (13i) \end{aligned}$$

where, $(X_1) = \frac{X_{Gelatin} - 5}{3}$; $X_{Gelatin} = arbitrary gelatin$ concentration.

(X₂) =
$$\frac{X_{Submith 2}}{X_{Softmed Alginute}}$$
 = arbitrary sodium alginate concentration.
(X₃) = $\frac{X_{Submith 2}}{X_{Softmed Alginute}}$ = arbitrary laponite concentration.

The response surface contour plots displayed in Figs. 2, 3, 4 illustrate how rheological and printability parameters change in response to variations in the concentrations (w/v) of the constituent biopolymers, namely Gelatin, Laponite and Sodium Alginate. In these plots, since the model con-siders the effects of all three input variables, when plot-ting two out of the three constituents, the third constituent remains fixed at the center of the tested concentration ranges. For example, in plots where a response variable is represented in relation to Gelatin and Laponite concentrations, the Sodium Alginate concentration is held constant at 3.5%. This approach allows us to visualize how changes in the concentrations of Gelatin and Laponite impact the response variable while keeping Sodium Alginate at a consistent level. Detailed perspective plots and contour plots with independent color ranges for each concentration are available in Supplementary Figures S4–S12.

Figure 2a–c illustrates the ZSV responses across differ-

ent concentration ranges of the raw constituents. In Fig. 2a, where the concentration of sodium alginate is fixed at 3.5%. an increase in gelatin concentration leads to higher ZSV val-ues, particularly at low laponite concentrations. This behav-ior can be explained by the microstructure formed by the electrostatic interactions among the edge-surface laponite platelets, which grant laponite its rheological modifier characteristics, including increased viscosity [16, 17]. However the presence of sodium alginate in the mixture hinders this "house of cards" structure formation in laponite [17]. To to the best of our knowledge, no linear correlation between viscosity and the concentration of specific constituents in the mixture system has been reported. Both sodium alginate and gelatin contribute to the rapid change in ZSV, as indi-cated by the model equation for ZSV and Figs. 2a, b. This is attributed to the ability of gelatin and sodium alginate to elevate system viscosities through mechanisms such as hydrogen bonding, polymer chain entanglements, and steric hindrance [80–85]. For laponites, the electrostatic repulsion in suspensions and layered-structure formation results in vis-cosity modifications [86]. However, in systems containing sodium alginate, the rheological-modification properties of

laponite such as ZSV is hindered as observed in the current

response such as 25 v is minuted as observed in the current experiment and also previous literature [16]. Figure 2d-f illustrates the response of the shear-thinning index as it relates to the constituent components. The figure demonstrates the shear-thinning behavior of the mixture system, as predicted by the CCD-RSM model. Figures 2d, f show a positive correlation between the shear-thinning index and the concentration of laponite. Laponite forms gels through surface charge interactions held together by weak van der Waals forces, which are easily disrupted by shear ing [87]. Therefore, in a system with a high concentration of laponite, the viscosity formed through such electrostatic attraction will rapidly decrease when subjected to shearing On the other hand, sodium alginate exhibits a negative cor-relation with the shear-thinning index, as seen in Fig. 2e and more prominently in Fig. 2f. Higher concentrations of sodium alginate result in an increased concentration of Na ions in the system, which masks the negative surface charge and reduces van der Waals attraction [88], thus diminishes the shear-thinning effect of Laponite in the system. Similarly, Gelatin also shows a negative correlation with the shear-thinning index due to the strong crosslinked gel net-work formed by the triple-helix structure at higher concen-trations, which resists shear deformations [89].

Figure 2g-i illustrates the maximum storage modulus (G') within LVER. Higher concentrations of laponite result in higher LVER-G' for all ranges of gelatin concentration, with sodium alginate (SA) concentration fixed. This is because laponite aqueous solution forms a stacked platelet structure that enhances mechanical stiffness [90, 91]. Addi-tionally, increasing gelatin concentration also contributes to higher LVER-G'. At room temperature (25 °C), higher concentrations of gelatin lead to a sol-gel transition, further enhancing mechanical stiffness within the LVER limit [92]. A plateau-like region shown in Fig. 2g indicates a drop in LVER G' at the intermediate gelatin concentrations between 3.5 to 6.5%. A similar trend is observed in Fig. 2h for varying gelatin concentration. In Fig. 2h gelatin demonstrates high LVER-G' at concentrations below 2.5% and above 7% with LVER-G' less than 1 kPa in the central plateau region. The sol-gel property of the mixture system depends on the concentration ratio between gelatin and any polysac-charide (sodium alginate). The stochiometric weight ratio changes the sol-gel transition temperature and forms additional junction zones in the gel network [93]. This affects the microstructure stability and changes the viscoelastic characteristics [93]. Prior literature shows non-linear trends of the storage modulus for changing gelatin and other polysaccharide (sodium alginate) concentration ratios [93, 94] Laponite demonstrated a consistent increase in LVER-G' values, approaching 1 kPa, with rising concentrations, particularly when combined with fixed gelatin and a low concentration of sodium alginate (less than 3.5%), as illustrated

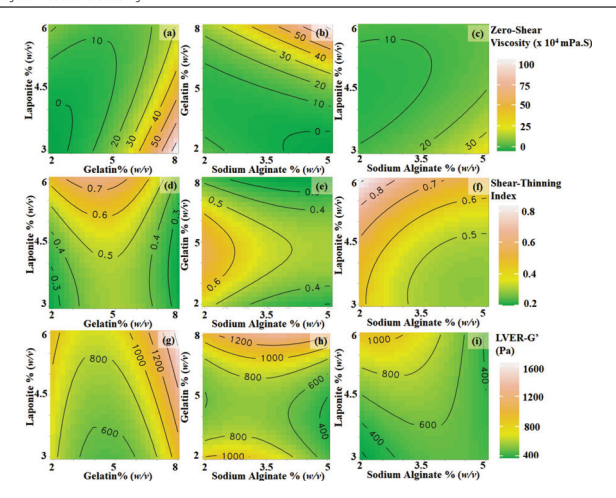


Fig. 2 Response surface contour plots for different gelatin, alginate, and laponite compositions for a-e ZSV, d-f STI, and g-i LVER-G

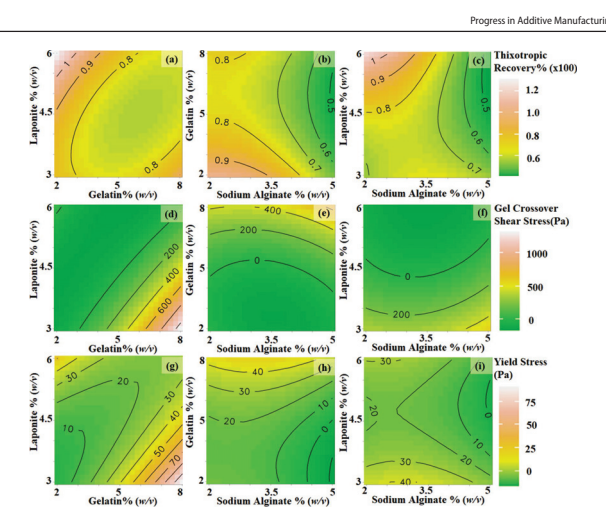
in Fig. 2i. Higher concentrations of sodium alginate interacts with laponite to disrupt the "house of cards" like layered structure that primarily gives Laponite it's high LVER G" [17]. The original amplitude sweep data used to construct the response surface data for the LVER-G' are provided in the Supplementary Figure S1.

Figure 3a—e show that high concentrations of laponite (>4.5%) combined with low gelatin concentrations (<3%) result in structures with 90% viscosity recovery within the first 5 s after experiencing high shear deformations. This rapid recovery of laponite viscosity aligns with findings from previous literature [95–97]. When subjected to shear forces, the microstructure of laponite dissociates into flocs or platelets but swiftly reorganizes into its initial structure following the removal of force [95]. However, higher concentrations of gelatin lead to reduced recovery rate at high laponite concentrations, as seen in Fig. 3a. For a fixed laponite concentration of 4.5%, Fig. 3b shows relatively high viscosity recovery rates (<75%) across all ranges of gelatin

concentrations and sodium alginate concentrations below 4.5%. This is attributed to the rate of disentanglement of adginate macromolecules outpacing their rate of re-entanglement, a phenomenon well-documented in previous studies [98]. Similarly, when gelatin concentration is 5%, a similar trend of high recovery rates (>>75%) is observed as shown in Fig. 3c. The original thixotropic recovery data used to construct the response surface data for the STI can be found in supplementary Figure S14.

Increased gelatin levels combined with reduced laponite concentrations necessitate greater stress to achieve the gelation point, as depicted in Fig. 3d. Laponite exhibits specific shear-thinning behavior, which contributes to the reduction in COST at higher concentrations [17]. On the contrary, higher concentrations of gelatin increase the glass transition temperature, melting point, and promote the formation of triple helix structures (physical aggregates) [99]. These factors lead to the formation of a densely packed network that is more resistant to shear forces, resulting in higher COST values [99, 100]. The inverse relationship between





 $Fig. 3 \quad \text{Response surface contour plots for different gelatin, alginate, and laponite compositions for a-e~THIX, d-f~COST, and~g-i~YSCOST, and~g-i~YSCOST,$

COST and laponite concentration, as shown in Fig. 3ef, can be attributed to the shear-thinning properties of laponite discussed earlier. The original amplitude sweep data used to construct the response surface data for COST are provided in Supplementary Figure S13.

Like the COST values, a high concentration of gelatin leads to a higher yield stress (> 70 Pa) at low laponite concentrations, as shown in Fig. 3g. However, increasing the laponite concentration at high gelatin concentration reduces the yield stress to less than 30 Pa for laponite concentrations above 5.5%. This reduction can be explained by the increased concentration of sodium ions with higher laponite concentrations [101] which in turn reduces the yield-stress as established in prior literature [31]. When both sodium alginate (SA) and gelatin concentrations are high, a maximum yield stress of 45 Pa is observed when laponite concentration is 4.5%, as shown in Fig. 3h. Figure 3i shows that with sodium alginate less than 3%, lowering the laponite concentration to tess than 3.5% increases

the yield stress, as there may be an insufficient number of phase-separating Na⁺ ions from laponite or alginate [102].

Figure 4a—c shows the swelling ratio response plotted against the mixture constituents. Laponite concentration exhibits an inverse relationship with the swelling ratio for different ranges of gelatin and sodium alginate concentrations. Higher laponite concentrations increase physical crosslinking and reduce the dissolution of the polymer in the solvent due to covalent interactions [103]. This effectively reduces the overall water uptake capacity of the hydrogel, leading to a lower swelling ratio. Furthermore, for a fixed laponite concentration of 4.5%, the swelling index decreases with increasing concentrations of both gelatin and sodium alginate. The triple-helix structure in the gelatin acts as a physical crosslink that resists solvent uptake, thereby reducing the swelling ratio[104]. Hence at higher gelatin concentrations, the polymer networks are more tightly packed that result in reduced swelling ratio [104]. A similar trend of reduced swelling ratio [104]. A similar trend of reduced swelling ratio gratio with

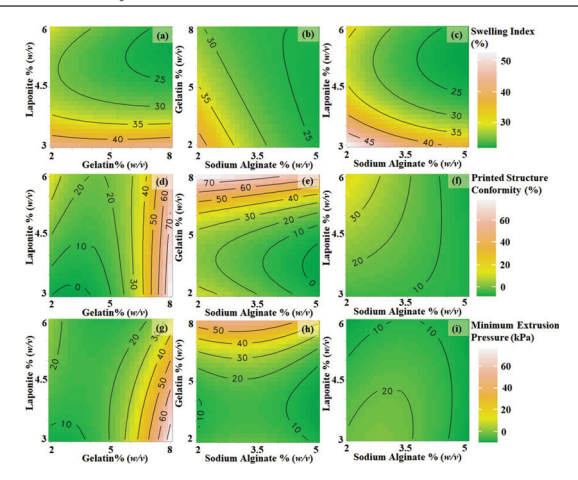


Fig. 4 Response surface contour plots for different gelatin, alginate, and laponite compositions for a-c SI, d-f PSC, and g-i MEP

increasing sodium alginate concentrations have been reported in prior literature [105] and can be attributed to the similar phenomena of packed polymer network density. Figure 4d-f shows that PSC is dominated by gelatin

Figure 4d-f shows that PSC is dominated by gelatin concentrations. Notably, even with the maximum laponite concentration of 6% and SA at a minimum of 2%, the highest achieved PSC is only 40%. From our current analysis of the PSC data, it becomes evident that a high gelatin concentration above 7.5% is desirable to achieve a PSC greater than 70% across various ranges of SA and laponite concentrations. Further details regarding the process and methodology for obtaining PSC are discussed in the upcoming Sect. 34.

upcoming Sect. 3.4.

Figure 4g-i shows the relationship between the MEP and bioink concentrations. For gelatin concentrations below 6%, the desired extrusion pressure (<30 kPa) is achieved when the laponite concentration is below 4.5%. In this range, the bio-ink exhibits a zero-shear viscosity of less than 30×10⁴ mPa·s (Fig. 4a) and a yield stress value of less than 50 Pa (Fig. 4g). The maximum extrusion

pressure (22 kPa) is observed at low laponite (<3.5%) and sodium alginate (<3.25%) concentrations, with gelatin fixed at 5.5%. This is due to the low values of ZSV (<15x 10⁴ mPa.S), LVER-G' (<600 Pa), and yield stress (<40 Pa) in this concentration range. Since our PSC data shows that the gelatin concentration needs to be above 7.5% to achieve high PSC, it is possible to adjust the minimum extrusion pressure to be less than 30 kPa by increasing the laponite concentration up to 6% and beyond, as indicated by the nonlinear trends in the contour plot in Fig. 4g. This possibility is further explored in the desirability function analysis section.

3.2 Bio-ink sol-gel characteristics

The results of the vial inversion test are presented in Fig. 5. It is evident that DP-3, 6, 7, 9, 10, 11, 12, and 14 display strong gel-like behavior, characterized by ZSV exceeding 15×10^4 mPa·s and yield stress over 20 Pa. DP-1 and 13 exhibit moderate levels of flowability, demonstrating



Progress in Additive Manufacturing

intermediate gel-sol transition characteristics, with ZSV ranging from 10 to 15×10^4 mPa·s and yield stress from 10-30 Pa. As for bioinks DP-2, 4, 5, 8, and 15 they display solution-like characteristics, featuring ZSV below 10^5 mPa·s and yield stress less than 5 Pa.

3.3 Bio-ink filament characteristics

The filament morphological information and images are presented in Fig. 6. DP-3, 6, 7, 11, 12, 13, and 14 show tubular filament characteristics. In all these bioinsk the LVER-G' was greater than 800 Pa, the ZSV greater than 10^5 mPa-s, and the yield point greater than 10 Pa. However, DP-6 and DP-12 showed higher filament diameter variability and average diameter owing to low THIX of 50% within the first 2 s following the extrusion process. Hence, based on the temporal and spatial stability, DP-3, 7, 11, 13, and 14 showed the least variability in filament diameter and the average diameter was closer to the nozzle diameter of approximately 0.5 mm. Hence the highest tubular-like filament conformity

was achieved when ZSV > 10^5 mPa·s, THIX > 75% within the first 2 s, Yield point > 10 Pa, and LVER-G' > 800 Pa.

3.4 Printed structure precision

We measured printed structure conformity using a 1 cm tall M-shaped 3D computer model with a 0.5 mm nozzle. As shown in Fig. 7, DP-2, 4, 5, and 8 did not form filaments. DP-3, 7, 11, and 13 had the best filament width and height conformity. However, DP-14, while stable, resulted in merged structures with poor width and height conformity due to under-gelation, possibly linked to its higher temperature-sensitive viscosity. The temperature-sicosity relation was determined by fitting viscosity data points obtained at a constant shear rate of 50 10 susing the Vogel power-law model [106] in the range of 20–40 °C. The temperature exponent constant as seen in the fitted power law equation in the supplementary Figure S15. Additionally, DP-3 exhibited over-gelation characteristics [107, 108] due to its higher temperature exponent constant as seen in the fitted power law equation in

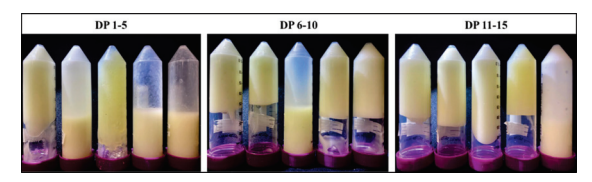


Fig. 5 The bioink flowability at room temperature (25 $^{\circ}\mathrm{C})$ after 60 s of vile inversion

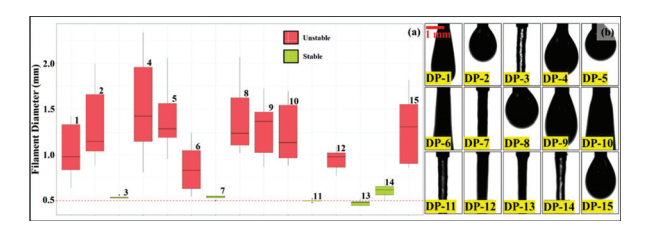
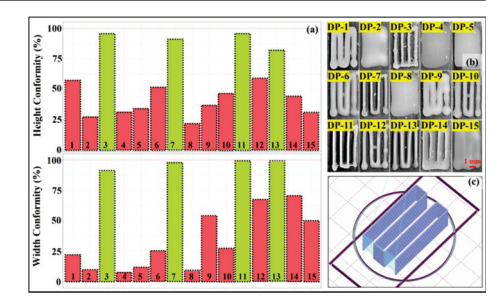


Fig. 6. a Filament diameter as an indicator of stability over different temporal and spatial points. b Filament in the near-field location of 10 mm from the nozzle for DP1 to DP-15

Fig. 7 a Printed structure height and width conformity (%) with respect to the original 3D model; Numbers inside the histogram bars indicate the design points (DP). Is Images of the printed structures for DP-1 to DP-15 c 3D model path used to inspect the conformity



yield stress (> 100 Pa) and high gel crossover shear stress (> 1100 Pa·s) values, despite its high structural conformity.

3.5 Desirability function analysis

In the target-ramp approach, desirability satisfaction parameters were introduced to bias the optimization process in a preferred direction. For example, the MEP target range was set from 5 to 40 kPa, with a low-scale value of 0.2 and a high-scale value of 1.5, as illustrated in Fig. 8. The optimizer will prioritize searching for optimal MEP values in the lower-scale region (approaching 5 kPa) to maximize the desirability index. Similarly, for PSC, we defined the target range from 80 to 100%, with a low-range scale factor of 3 and a very small low-scale value of 0.0001. The optimizer will focus on finding optimal PSC values between 80 to 100%, with a stronger emphasis on values closer to 100%. Regarding LVER-G', we used a maximization range with a scale factor set to 2, ranging from 1100 up to a variable upper limit. The minimum value of 1100 P for LVER-G' was chosen based on experimental observations that resulted in good structural integrity.

The targets for MEP and PSC, and the upper limit of

The targets for MEP and PSC, and the upper limit of the LVER-G' were iteratively generated using a loop function, as illustrated in Fig. 8d. The value-generating loop function was nested under an outer loop function that also encompassed the desirability functions. The generative loop function dynamically produced values for parameters a, b, and c. As a result, we obtained multiple optimal compositions for the bioinks that met the criteria of $5 \, \text{SMEP} \, \text{S4}, 0.8\% \, \text{SPSC} \, \text{S} \, 100\%$, and LVER-G' $\text{S} \, 1100 \, \text{Pa}$. By implementing this expanded grid search, we extended our solution points beyond the range tested in the experiments. This

allowed us to maximize the desirability of multiple objective functions and identify a broader set of solutions. The desirability equations with the user-specified search parameters are presented in supplementary section as Equations S1a-d.

Based on the optimality search, we classified solutions

Based on the optimality search, we classified solutions into five different categories with their corresponding characteristics, constituent materials, response values, and desirability index D as shown in Table 1. Following our optimization approach, we designated OP-5 as the ideal solution, which combines high LVER-G' (> 1100 Pa), high PSC (> 90%), and low MEP (< 30 kPa). Supplementary Table S2 presents the differences between the predicated valutes and experimental values, demonstrating the good performance of our models. Figure 9 presents PSC and qulitative images of different sutrucres printed using OP-5.

3.6 Printability performance of the optimized

Figure 10 shows the filament collapse test results for OP-5. At the printing speed of 20 mm/s, the filaments exhibit the least deformation. Conversely, lower printing speeds lead to a higher volume of filaments deposited per unit length, causing them to yield more under their own weight. Figure 10f summarizes the collapse area factor under different gaps, speeds, and time intervals after filament depositions. For gaps greater than 10 mm, significant statistical differences (t-test) were found when speed varied. At the optimal printing speed, our optimized bioink demonstrates approximately 7.5 times better resistance against filament collapsing compared to previous results using oxidized alginate-gelatin bioinks reinforced with low laponite concentrations [102].





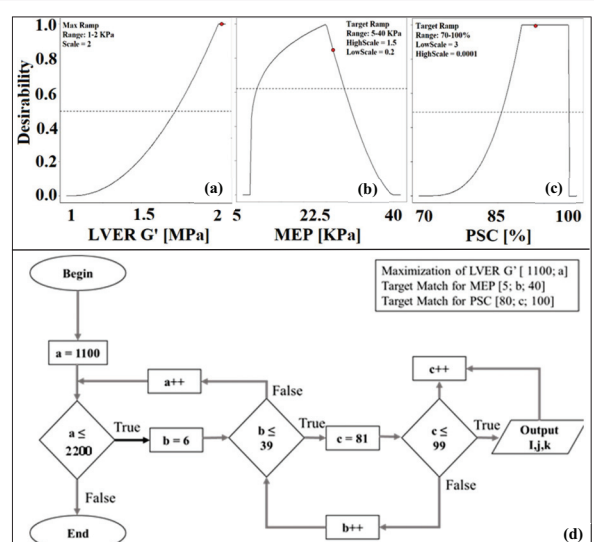


Fig. 8 The desirability ramp and parameters to optimize the multiresponse-objective (MRO) problem. a Maximization ramp for LVER-G'b target-ramp for MEP and c target-ramp for PSC. Red dot indi-

cates optimal responses from DFA for OP-5 d the looped iterative search for an optimal max or target value for the MRO problem

Table 1 Sets of 5 optimal points obtained by DFA optimization

Optimal points	Characteristics	Gel	SA	Lap	LVER G' limiting var (a)	MEP target var (b)	PSC target var (c)	D
OP-1	High PSC	8.49	6.56	2.56	1100	26	99	0.98
OP-2	High LVER-G'	9.57	5.31	6.44	1900	36	80	0.94
OP-3	Low MEP High PSC	8.26	6.67	2.09	1100	18	96	0.99
OP-4	High PSC High LVER	9.42	6.41	4.72	1500	36	96	0.97
OP-5	High PSC High LVER Low MEP	8.69	2.31	6.73	2200	28	90	0.99



Fig. 9 a Top view and b side view of a zig-zag structure with the bioink compostion at the optimal point (OP-5), c Isometric view and d Side view of a thin-walled (-0.5 mm) cylindrical structure with the bioink compostion at the Optimal Point (OP-5) (14 layers with

0.5 mm/ layer). e Isometric g front (focused) f top and h front (full) view of a 3-layered 2 cm long tubular structure printed with OP-5. i Side and j isometric view of a meniscus model printed with OP-5. OP-5 in e-j color textured using 0.2% (v/v) red dye (Allura Red AC)

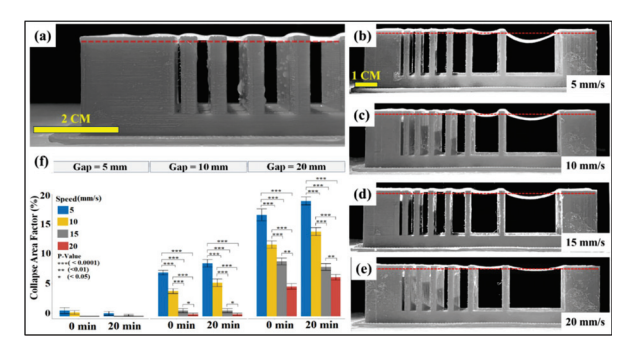


Fig. 10 a Uncollapsed structure in low pillar gaps (1–5 mm), collapse characteristics for a traversing speed of b 5 mm/s c 10 mm/s d 15 mm/s e 20 mm/s. f Collapse Area Factor percentage plotted for different printing speed, wall gap, and time

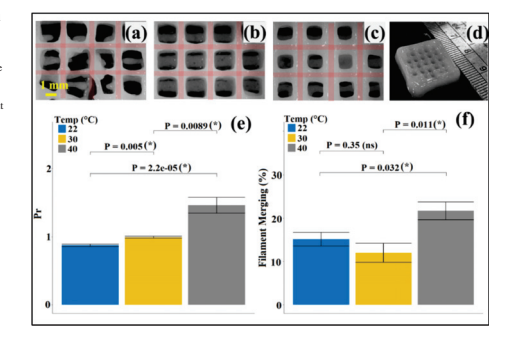
Figure 11 shows the filament merging and printability index of OP-5. At room temperature, the filaments exhibit over-gelatin characteristics, leading to broken grid structures. When the temperature is set to 30 °C, the filaments align well and exhibit morphology matching with the 3D design. However, at higher temperatures (40 °C), the bioink begins to display under-gelation characteristics,

resulting in the formation of thick printed filaments. Analysis of variance (ANOVA) followed by t-tests reveals significant statistical differences in the printability index of the optimal bioinks printed at different temperatures. Printing at 30 $^\circ$ C yields the best printability index. To sum up, a printing speed of ~ 20 mm/s at 30 $^\circ$ C resulted in the best printability performane.



Progress in Additive Manufacturing

Fig. 11 The filament merge and printabilit index for different temperatures using OP-5 at a 22 °C b 30 °C e 40 °C. d The isometric view of the grid shape formed at 40 °C. e The printability index (Pr) and filament merging (%) of OP-5 at different temperatures



3.7 Post-extrusion cell viability

GFP-HUVEC were mixed in the OP-5 bioink and printed in a single layer with thickness of 0.5 mm. The extrusion pressure was set at 35 Kpa with nozzles heated to 37 °C to minimize thermally induced cellular death. The live-dead staining of the cells in this printed bioink are presented in Fig. 12. High cellular viability, averaging 93%, was

confirmed through image analysis across multiple (n = 5) images. Consequently, due to the low extrusion pressure provided by the optimized bio-ink, it can be affirmed that the shear-induced forces experienced by the cells in the bioink result in less than 7% cell death.

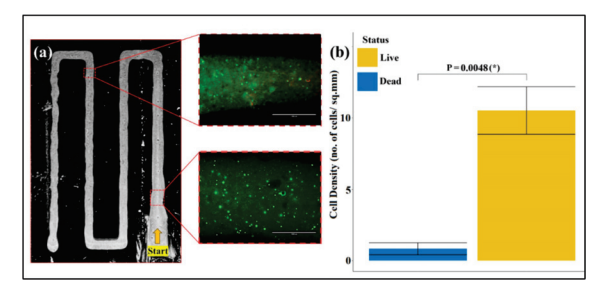


Fig. 12 a RFP and GFP overlaid images in different regions of a 0.5 mm printed layers. b Statistical information on the Live/ Dead cell distribution in the printed structure

3.8 Machine learning based response modeling

We used the neural network model to establish a non-linear regression relationship between the rheological and printability parameters. The predicted versus actual PSC and MEP responses using the rheological predictors are shown in Fig. 13. The strong correlation between predicted and actual values demonstrates the reliability of our MEP and PSC models. The hyperparameters of the machine learning model, including the number of layers, activation functions, learning rates, epochs, batch size, layer drop rate, regularization factor, and scheme, were selected through iterative improvements, resulting in reduced model errors. No specific hyperparameter optimization scheme was implemented for the learning rate. In this experiment, we explored the MEP and PSC trends by varying LVER-G' while keeping the other rheological parameters fixed at their optimal solution values (OP-5).

Figures 14 and 15 illustrates how PSC and MEP vary with rheological parameters LVER-G² and COST. Figure 14a shows that PSC positively correlates with LVER-G² but remains relatively stable with COST. However, at low LVER-G² values (1000 Pa), inconsistent PSC is observed, with significant drops occurring at high COST (>750 Pa). It could be attributed to the fact that at low LVER-G², bioinks that require high shear stress to undergo gel-sol transition may show over-gelation behavior [65, 109] resulting in reduced structural integrity. The MEP shows a positive correlation with COST for LVER-G² > 1200 Pa as shown in Fig. 15a. With the increase in the COST, the viscoelastic bioink requires a higher amount of shear stress to go through the gel-sol transition [110]. Increasing COST leads to higher extrusion pressure. As LVER-G² levels rise from 1000 to 2000 Pa, MEP consistently increases, in line with prior literature [41]. These MEP and PSC predictions apply when the biomaterial has specific properties, including a

shear-thinning index of 0.38, thixotropic recovery rate of 94%, yield stress of 29.07 Pa, and ZSV of 22.28×104 Pa, as defined in the optimal solution OP-5

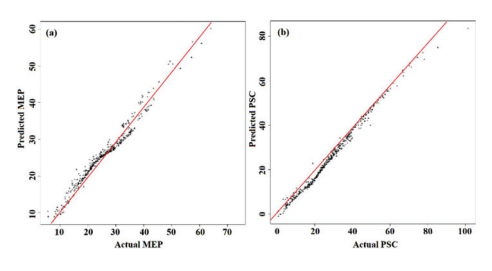
as defined in the optimal solution OP-5.
Figure 14b and 15b present the effects of STI and LVER-G' on PSC and MEP, respectively, PSC positively correlates with both LVER-G' and STI. Bioinks with good shear-thinning properties exhibit high printability, reducing nozzle clogging, enabling precise deposition, and ensuring smooth extrusion [46, 111, 112] especially at sufficient LVER-G' levels. But STI has a negative correlation with MEP across the entire LVER-G' range. This is because an increase in the shear-thinning index leads to a reduction in yield stress [113, 114] subsequently lowering the MEP required to extrude the bioink from the nozzle at a fixed LVER-G'. These MEP and PSC predictions for different STI and LVER-G' values are valid under the condition that other rheological values (ZSV, COST, YS, and THIX) remain fixed at their optimal solution values in as in OP-5.

Figure 14c and 15c show the interactions of yield stress and LVER-G'. The increase in PSC alongside higher yield stress can be ascribed to the structure's enhanced resilience against deformations and collapses. This is due to the necessity for greater shear stress to initiate flow in viscoelastic materials, a concept previously discussed. Moreover, MEP shows a markedly positive correlation with yield stress across increasing LVER-G' intervals. This aligns with established literature, indicating that yield stress is a primary determinant of extrusion pressure for specific nozzle

across increasing LVER-G' intervals. This aligns with established literature, indicating that yield stress is a primary determinant of extrusion pressure for specific nozzle sizes [115].

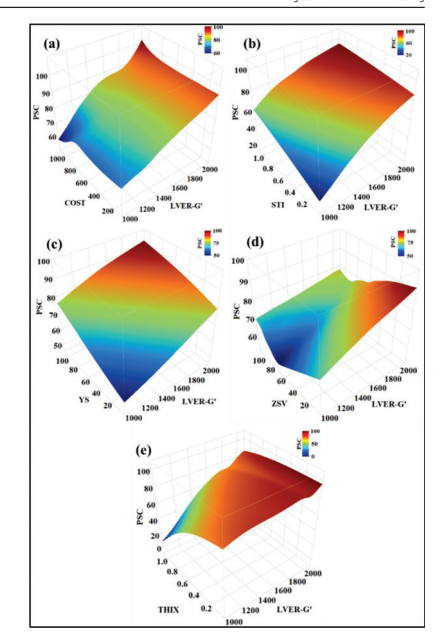
In Fig. 14d, PSC decreases as ZSV increases when LVER-G' < 1600 Pa because of the higher loss modulus and a lower storage modulus [116]. Consequently, the drop in the storage modulus leads to decreased PSC. Beyond a ZSV threshold of 60 x 104 mPa.s, PSC begins to rise again, as viscous forces become strong enough to counteract flow deformations, thus preserving structural integrity [20,

Fig. 13 Predicted vs test data for a PSC and b MEP



Progress in Additive Manufacturing

Fig. 14 Response surface plots showing the response of PSC for LVER-G' vs a COST b STI c YS d ZSV and e THIX



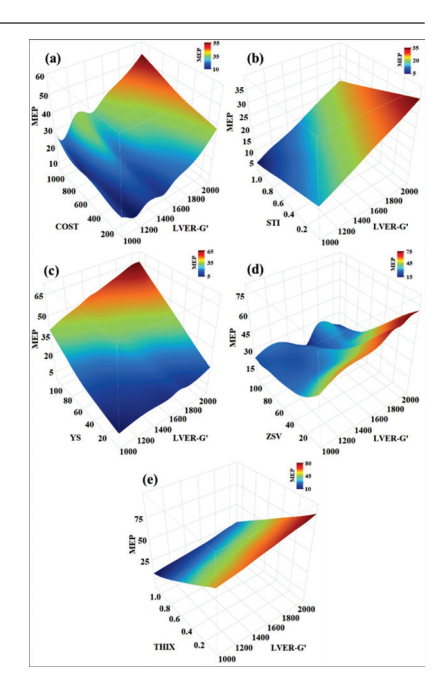
117–119]. As demonstrated in Fig. 15d, MEP negatively correlates with increasing ZSV; a higher ZSV, for a fixed complex viscosity, implies a greater loss component and lesser elastic component [41]. Consequently, the material tends towards more viscous behavior with enhanced flowability and lower MEP. However, at extremely high ZSV values above 30 x 10⁴ mPa-S, the minimum extrusion pressure plateaus, indicating no further decrease.

Figure 14e and 15e illustrate how the PSC) and MEP vary with changes in the THIX and LVER-G: At LVER-G' values below 1400 Pa, an increase in THIX leads to a marked decrease in PSC, indicating that higher THIX may

produce more viscous-dominant gels with increased yielding behavior, thus reducing stiffness and PSC [120]. While there is a negative correlation between MEP and THIX across all LVER-G' levels. This is likely due to these materials' enhanced ability for micro-structure polymer chain network reconstruction [121]. In conditions where other rheological parameters are constant, materials with higher THIX may exhibit rapid polymer structure breakdown under low external force, contributing to lower MEP. These observations, derived from data mining techniques, are specific to conditions where other rheological properties are maintained constant for the OP-5.



Fig. 15 Response surface plots showing the response of MEP for LVER-G' vs a COST b STI c YS d ZSV and e THIX



3.9 Discussion and future perspectives

To demonstrate the capability of our ANN model on bioinks containing materials other than Iaponite, gelatin, or alginate, we utilized corn, potato, and rice starch mixed at varying concentrations. We determined the rheological parameters and proceeded with PSC and MEP determination, employing the same procedure as applied to our experimental bioinks. The results indicate prediction accuracies exceeding 82% and 89% with average of 85.4% and 89.7% for MEP and PSC, respectively, as presented in supplementary Table S3.

Supplementary Figure S20 provides images of the printed structures. These models are exclusively applicable to bioinks where all six input predictors can be ascertained. For bioinks lacking any of these rheological parameters, accubronins tacking any of these incongectar parameters, accurate determination of PSC and MEP data becomes challenging. For instance, we tested aqueous solutions of 15% (w/v) polyethylene oxide (PEO), which exhibited no characteristic yield point or cross-over shear stress features, resulting in a low PSC, as depicted in supplementary Figure S20j, k. Our ANN models do not accept 'Null' values in any of the six input nodes. Therefore, we assigned a very small value



(0.1 Pa) to determine the PSC and MEP values. This led to

diminished prediction accuracies for both PSC and MEP.

Bioprinting has recently witnessed remarkable progress propelled by various machine learning techniques, including convolutional neural network models for image data, process optimization, tool path planning, prediction of cellular behavior and viability, quality detection, and data pattern analysis, among others [122–134]. Our work demonstrated the excellent performance of the ANNs in predicting the intricate relationships between rheological properties and printability parameters (MEP and PSC). In addition, we applied a linear regression model to the primary dataset, focusing solely on the main effects (rheological paramrectising solely on the main elects (incongical parameters) and excluding interactions, quadratic, or higher-order terms related to printability parameters. Although the linear regression model resulted in a relatively modest R-squared value, it still affirmed the overall positive and negative cor-relations observed in our ANN models. Although the proposed modeling technique is designed for tissue engineering scaffold applications, the rheology-

based printability and extrusion force modeling technique can be extended to other areas of extrusion-based processes that involve viscoelastic materials. For example, metal particles embedded in biodegradable hydrogels have been utilized as 3D printable materials, followed by sintering to produce metallic components [135], flexible electronics, and polymer-based transducers [136, 137]. The printability performance of these materials is significantly influenced by the rheological properties of the metal-embedded organic inks, which can be predicted using the proposed modeling techniques. 3D printing is also employed in digitization and controlled nutrition distribution in food products [138] or viscoelastic drug design [139]. In such cases, predictions of print quality based on ingredient rheology can play a crucial

In terms of biocompatibility, this paper only assessed the immediate cell viability after printing. Even though the gelatin-alginate formulation has extensively researched for its ability to improve proliferation and cellular attachment across diverse cell types [140, 141], future studies should focus on the long-term cell viability and proliferation in this hybrid bioink. Cell attachment and proliferation rates are dependent on a range of factors including hydrophilicity, hydration levels, pore sizes, polymer chain density, and the degree of crosslinking. These properties can be further opti-mized by integrating bioactive additives. Subsequently, the printability prediction model using ANN, as demonstrated in this paper, can be effectively utilized to assess printability parameters influenced by these altered rheological char-acteristics. Future research will also expand these machine learning models by integrating nozzle and syringe specifications as labeled data, thereby enhancing their applicability to a wider array of scenarios. Moreover, to refine bio-ink

formulation, it will be essential to model and optimize a tornination, it will be essentiant to moder and optimize-series of operational parameters, including flow rate, print-ing speed, and layer height. These approaches in optimiza-tion and predictive modeling hold substantial potential for advancing the field of bioprinting as a whole.

4 Conclusion

This paper presented a systematic methodology for determining the material composition ratios of multi-material bioinks to achieve optimal printability. It established a general correlation between the rheological properties of general contrainmon between the incongent appetertes bioinks and their printability, irrespective of the specific bioink composition. Specifically, the study investigates various rheological and printability parameters, including zero-shear viscosity, maximum storage modulus within the linear viscoelastic region (LVER), cross-over shear stress (COST), yield stress, printed structure conformity (PSC), and extrusion pressure. The results demonstrated positive correlations with gelatin concentration for most parameters, while gelatin exhibited negative correlations with the shear-thinning index, thixotropic recovery rate, and swelling index. Sodium alginate concentration displayed a positive correlation with zero-shear viscosity and cross-over shear stress but negatively influenced other rheological and printability parameters. The addition of laponite enhanced the printed structure integrity and reduced extrusion pressure. Based on the proposed model, the optimal bioink formulations for on the proposed moder, the opinian from the formation of popular optimal printability featured high gelatin (> 8%) and laponite (> 6%) concentrations but low sodium alginate (< 2.5%) concentration. The optimal solution has a cross-over shear stress of 178 Pa, yield stress of 29 Pa, a high viscosity thixotropic recovery of 94%, a shear thinning index of 0.38 (Ostwald de Waele power-law model).

Furthermore, an artificial neural network data mining approach revealed general correlations between various rheological parameters and extrusion pressure. The cross-over shear stress demonstrated, and yield stress exhibited positive correlations with MEP across all LVER-G' ranges. Conversely, the shear-thinning index and zero-shear viscosity were negatively correlated with MEP. LVER-G' demonstrated a strong positive correlation with MEP and PSC across all combined rheological factors. According to our model, bioinks with a higher shear-thinning index > 0.30, yield stress > 20 Pa, a thixotropic recovery rate > 85%, zero-shear viscosity > 20 × 10⁴ mPa.s, and a LVER-G value > 1200 Pa will result in high PSC of over 90%. Meanwhile, it is essential to keep the yield stress < 80 Pa, thixo-tropic recovery rate > 60%, and LVER-G' ranging from 1200 to 2200 Pa to make the MEP less than 35 Kpa, which is the upper limit for cell viability. The models predicting PSC and MEP demonstrated high accuracy, with MAE) of up to 6.3%

for PSC and 8.1% for MEP in the tested composite bioink materials. For other structured fluid materials not included in the training set, the models achieved average MAEs of approximately 10% for PSC and 14.6% for MEP. This demonstrates the versatility and the strength of ML-based modelling approaches in bioprinting applications. Future investigations are required to build models with higher pre-diction accuracies involving training with greater number of predictors, wider range of rheology and concentration data, flexible number of predictor inputs, and different biomaterials to develop a universally applicable model. Furthermore, formulation of ingredients, strategies, and modeling techniques for connecting long-term culture viability, spreading, and proliferation with the immediate post-fabrication viability can be explored to develop a standardized high-fidelity bioink with long-term cell sustaining capability. In summary, this study provides valuable insights into

the rheological and printability behavior of gelatin-laponite sodium alginate-based bioinks. The results provide es insights for choosing the right rheological parameters, based on the composition of materials, to enable the creation of high-fidelity bioprinted structures. These parameters are retrucial for establishing optimal extrusion conditions that minimize cellular damage. This work lays the foundation for future endeavors aimed at improving bioink formulation and optimization techniques and machine learning approaches for extrusion-based bioprinting in the creation of cell-incor-porated hydrogel tissue scaffolds.

Supplementary Information The online version contains supplementary material available at https://doi.org/10.1007/s40964-024-00828-1.

Acknowledgements This work was supported by the National Science Foundation under grant number xxx.

Author contributions Study conception and design, project management: George Z. Tan. Experiment, analysis and interpretation of results, draft manuscript preparation: Imitaz Qavi. Experiment and data collection: Sampa Halder. All authors reviewed the results and approved the final version of the manuscript.

Funding This work was supported by National Science Foundation, 2145108, George Tan.

Data availability The datasets generated in this study are available from the corresponding author on request.

References

- Pati F, Gantelius J, Svahn HA (2016) 3D bioprinting of tissue/ organ models. Angew Chem Int Ed 55(15):4650-4665
 Yilmaz B, Tahmasebifar A, Baran ET (2020) Bioprinting tech-
- Joseph Marketta Marke 279-319

- 3. Zhu W et al (2016) 3D printing of functional biomaterials for tissue engineering. Curr Opin Biotechnol 40:103–112
- Atu w et al (2016) 3D printing of functional biomaterials for tissue engineering. Curr Opin Biotechnol 46:10-31.
 Gu BK et al (2018) 3D bioprinting technologies for tissue engineering applications. Inc Unut H. Park CH, Kwon BK, Khang G (exh) Cutting-edge enabling technologies for regenerative medicine. Springer. Singapore, p. 15-28
 He Y et al (2020) Why choose 3D bioprinting? Part II: methods and bioprinters. Springer, Cham, pp. 1-4
 Ning L. Chen X (2017) A brief review of extrusion-based tissue scaffold bio-printing. Biotechnol 12(8):160067
 Gebeychu A et al (2021) Polysaccharide hydrogel based 3D printed tumor models for chemotherapeutic drug screenig. Sci Rep 11(1):372
 Silva C et al (2020) Rational design of a trind-lowered coxxist

- Rep 11(1):372

 Silva C et al (2020) Rational design of a triple-layered coaxial
- Silva C et al (2020) Rational design of a triple-layered coaxial acturader system: in silico and in vito evaluations directed toward optimizing cell viability. In J Bioprint del-(2)22.
 Axpe E, Oyen M. (2016) Applications of algitate-based bioinks in Disopriming. In J Mol Sci J 71(2):1976
 Wa Z et al (2020) In vitro and in vivo biocompatibility evalua-sion of the companion of the companion of the companion of the scaffold. Mater Sci Eng. C 109:110530
 Labowska MB et al (2021) A review on the adaption of algi-nate-gelatin hydrogels for 3D cultures and bioprinting. Materials 14(4):838

- Labowska MB et al (2021) A review on the adaption of alginate-gelatin plydrogels for 3D cultures and bioprinting. Materials 14(4):858
 Wang X et al (2017) Gelatin-based hydrogels for organ 3D bioprinting. Polymers (90):401
 Mota A et al (2014) Human bone marrow mesenchymal stem cell behaviors on PCL/gelatin nanofibrous scaffolds modified with a collagen IV-derived RGD-containing peptide. Cell J 16(1):1
 Tomás H, Alves CS, Rodrigues J (2018) Laponite®: A key nanoplatform for biomedical applications? Nanomed Nanotechnol For biomedical applications? Nanomed Nanotechnol Bold 14(7):2407–2420
 Afewerki S et al (2019) Bioprinting a synthetic smectic clay for orthopedic applications. Adv Healthcare Mater 8(13):1900158
 Daivila JL, d'Avila MA (2019) Rehoolgical evaluation of Laponite/alginate inks for 3D extrusion-based printing. Int J Adv Muntf Technol 101:675–686
 Divila JL, d'Avila MA (2017) Laponite as a rheology modifier of alginate solutions: physical gelation and aging evolution. Capture of alginate bouttons: physical gelation and aging evolution. Capture of alginate bouttons: physical gelation and aging evolution. Capture of alginate bouttons: physical gelation and aging evolution. Capture 10:1075–686
 Bovita JL, d'Avila MA (2017) Laponite as a rheology modifier of alginate bouttons: physical gelation and aging evolution. Capture 10:1075–686
 Bovita JL, d'Avila MA (2017) Laponite as a rheology modifier of alginate bouttons: physical gelation and aging evolution. Capture 10:1075–1074
 Bown JA, Porter MJ, Williams CB (2023) A rheology of inks for extrusion-based 3D bioprinting. Bioprinting 22:e00129
 Schush A et al (2010) Divisible soft boxed feature of biorists.

- Amorim P et al (2021) Insights on shear rheology of inks for extrusion-based 30 hiporitania; Beptirating 22-2001 20
 Schwich A et al (2020) Printability and shape fidelity of bioinks in 3D hipprinting, Chem Rev 12001/91/1028-1105
 Patton N et al (2017) Proposal to assess printability of bioinks for extrusion-based hipprintial and evaluation of rheological properties governing bioprintiability, Biofabrication 94(3)-041/07 22. Townsend M et al (2019) Flow behavior pior to crossilisting: the need for precursor rheology for placement of hydrogels in medical applications and for 3D bioprinting. Prog Polym Sci 91:26-140
 Ouyang L (2022) Pushine the shape first of the properties of
- Ouyang L (2022) Pushing the rheological and mechanical boundaries of extrusion-based 3D bioprinting. Trends Biotechnol
- boundaries of extrusion-based 3D bioprinting. Trends Biotechnol 40(7):891–8022

 24. Ramesh S et al (2021) Extrusion bioprinting: recent progress, etal-lenges, and future opportunities, Bioprinting: 21:e016

 25. O'Connell C et al (2020) Characterizing bionisk for extrusion bioprinting printability and rheology. Methods Mol Biol 2140:111–132.
- 2140:111-133 Myers RH, Montgomery DC, Anderson-Cook CM (2016) Response surface methodology: process and product optimiza-tion using designed experiments. John Wiley & Sons, Hoboken



Progress in Additive Manufacturing

- Whitcomb PJ, Anderson MJ (2004) RSM simplified: optimizing processes using response surface methods for design of experi-
- processes using response surface methods for design of experi-ments. CRC Press, Boca Raton
 Talib NAA et al (2017) Optimization of peak current of poly (3,
 4-ethylenedioxythiophene/multi-walled carbon nanotube using response surface methodology/central composite design. RSC
- merciew on its applications and challenges in microbial cuttures.

 Mater Today Proc 42:2277–2284

 Ferdosian F et al (2014) Synthesis of lignin-based epoxy resins:
- optimization of reaction parameters using response surface meth-odology, RSC Adv 4(60):31745-31753 Sheikhi A et al (2018) Effect of ionic strength on shear-thin-ning nanoclay-polymer composite hydrogels. Biomater Sci (48):2072: 3078

- Sheibhi A et al (2018) Effect of ionic strength on shear-thin-ning nanoclay-polymer composite hydrogels. Biomater Sci 6(8):2073-2083
 Gladukh I, Podorozhan M (2021) Study of structural and mechanical properties of sodium alginate gels. EUREKA Health Sci. https://doi.org/10.2130/3504-5679-2021.001732
 Saarai A et al (2013) On the development and characterisation of crosslindes odnium alginate/gelatine hydrogels. J Mech Behav.
 Krüger-Genge A et al (2012) Response of endothelial cells to gelatin-based hydrogels. ACS Biomater Sci Eng 7(2):527-540
 Krüger-Genge A et al (2012) Response of endothelial cells to gelatin-based hydrogels. ACS Biomater Sci Eng 7(2):527-540
 Tamg-Quan KR et al (2020) Gelatin promotes cell retention within deceillularity beart central production of active ystage bone-material methods of the structure of the structure of the structure of the structure and within deceillularity and the structure of the s

- Munoz-Perez E et al (2023) High resolution and Indelty 3 D printing of Laponice and aliginate in Mystogesle for tunable biomedical applications. Biomater Adv 149:213414
 Dong L et al (2021) Facile extrusion 3D printing of gelatine methacrylate/Laponite nanocomposite hydrogel with high concentration nanoclary for bone tissue regeneration. Int J Biol Mac-
- centration nanoclay for bone tissue regeneration. Int J Biol Mac-romol 188:72–81

 Müller SJ et al (2020) Flow and hydrodynamic shear stress inside a printing needle during biofabrication. PLoS ONE 15(7):e0236371
- 15(7):e0236371
 Balani SB et al (2019) Influence of printing parameters on the stability of deposited breats in fused filament fabrication of poly (factiv) acid. Addit Manuf 25:11-28
 Beran T et al (2018) Nozzle clogging factors during fused filament fabrication of spherical particle filed polymers. Addit Manuf 25:206-214
- Manuf 23-206-214
 Vajravelu K, Prasad K, Ng C-O (2012) Unsteady flow and heat transfer in a thin film of Ostwald-de Waele liquid over a stretching surface. Commun Nonlinear Sci Numer Simul 17(11)-4163-4173
 Kng J, et al. (2022) Suspension medium-based 3D bioprinting technology and fabrication of thin microfiber and porous

- structure using a decellularized extracellular matrix (dECM) bioins. 용 근 정 및 금 원의 물 속 발 표 대 원 문 장 .p. 102-102

 49. Gorjan L. et al (2020) Effect of stearie acid on rheological properties and printability of ethylene vinyl actact has based (edatocks for fused filament fabrication of alumina. Addit Manuf 36:101391

 50. Costaks W Jr et al (2016) Additive manufacturing of boron carbide via continuous filament direct nik writing of aqueous ceramic suspensions. J Eur Ceram Soc 36(14):2240-3256

 51. Thakare K et al (2021) Bioprinting using algae: effects of extrusion pressure and needle diameter on cell quantity in printed samples. J Manuf Sci Eng 143(1):014501

 52. Aguado B Ac al (2012) Imporying viability of stem cells during syringe needle flow through the design of hydrogel cell carriers. Tissue Eng Part A 187(-8:806-815)

 53. Agashi K, Chan DY, Shakesheff KM (2009) The effect of delivery via narrow-bore needles on mesenchymal cells. Regen Med 54. Touré AB, Mele E, Christie JK (2020) Multi-layer scaffolds of propost manufactured by combine 3d printing and electrospinning. Nanomacricals (10)(4)(2): 95.

 55. Fang Y et al (2023) Engineering highly vascularized bone tissues by 3D bioprinting of granular prevascularized spheroids. ACS Appl Mater Interfaces 15(37):43492-43502

 56. Bertuola N et al (2021) Celtain-aligniase-hyaluronic acid inks for 3D printing-effects of bioglass addition on printability, rheology and scaffold tensile modulus. Mater Sci 56(27):15327-15349

- Bertuola M et al (2021) Gelatin-atginate-myanuonic axis insta-3D printing: effects of bioglass addition on printability, rheology and scaffold tensile modulus. J Mater Sci 56(27):15327–15343 Kang K, Hockaday L, Butcher J (2013) Quantitative optimization of solid freeform deposition of aqueous hydrogets. Biofabrication Park H et al (2009) Effect of swelling ratio of injectable hydro-

- rabbit marrow mesenchymai seus seus composition (103/541-364).

 Zhang Het al (2018) Ionic effects on the mechanical and swelling properties of a poly (acrylic acid/acrylamide) double crosslinking hydrogel. New J Chem 42(11)9151-9158.

 Amdoun Ret al (2018) The destinability optimization methodology: a tool to predict two antagonist responses in biotechnological systems: case of biomase growth and possegumic content and second 16(1):e1339 Kuhn M (2016) The desirability package. Recuperado de http://
- crans-project.org/web/packages/desirability/vignetee/desirability/gdf. Accessed 2 Dec 2020 62.

 Lee DH, Jeong JJ, Kim KJ (2018) A desirability function method for optimizing mean and variability of multiple responses using a posterior preference articulation approach. Qual Reliab Eng Int 34(3):360–370 Printability' of candidate biomaterials for extrusion based 3D printing: state-of-the-art. Adv Healthcare Mater 6(16):1700/264

 61. Habib A et al (2018) 3D printability of alginate-carboxymethyl cellulose hydroged. Materials 11(3):454

 62. Ouyang L et al (2016) Effect of bioinfs properties on printability and cell viability for 3D bioplotting of embryonic stem cells. Biofabrication (8(3):03500)

 66. Ross-Murphy SB (1992) Structure and rheology of gelatin gels: recent progress. Polymer 33(12):2622–2627

 67. Al Hazza MH, Saadah AH (2019) Flank wear modeling in high speed hard end milling using integrated approach of Monte Carlo

- AI TAZZA MIT, SASIALI AT (2017) TIAIR Weat intolocing in ingg speed hard end milling using integrated approach of Monte Carle simulation method and Taguchi design. In: 2019 internationa conference on electrical and computing technologies and applica-tions (ICECTA), IEEE

- Khayyam H et al (2020) A novel hybrid machine learning algorithm for limited and big data modeling with application in industry 40. IEEE Access 8:11381–11393
 Khayyam H, Golkarnarenji G, Jazar RN (2018) Limited data modelling approaches for engineering applications. In Nonlinear approaches in engineering applications. In Nonlinear approaches in engineering applications. energy, vibrations, and modern applications p. 346–379
 Hussain MZ, Khan S, Sarmah P (2020) Optimization of power of the control of the
- Hussain MZ, Khan S, Sarmah P (2020) Optimization of powder metallurgy processing parameters of Al₂O/Gu composite through Taguchi method with Grey relational analysis. J King Saud Univ Eng Sci 32(4):274–286
 Briscoe E, Feldman J (2011) Conceptual complexity and the bias/variance tradeoff. Cognition 118(1):2–16
 Yang Z, et al. (2020) Rethinking bias-variance trade-off for generalization of neural networks. In: international conference on machine learning, PML
 Gulli A, Pal DS (2017) Deep learning with Keras. Packt Publishing Ld, Birmingham

- Juni A, ral DS (2011) Deep learning with Keras. Packt Publishing Ltd, Birmingham
 Joshi S, et al. (2021) Analysis of preprocessing techniques.
 Keras tuner, and transfer learning on cloud street image data.
 In: 2021 IEEE international conference on big data (big data), IEEE
- 75. Karlik B. Olgac AV (2011) Performance analysis of various

- 1 IEEE
 1 ISEE
 1 ISEE
 2 ISEE
 2 ISEE
 3 ISEE
 3

- Stat Softw 32:1–17

 Stat Softw 32:1–17

 Stat Softw 32:1–17

 Stat Softw 32:1–17

 State 32:1–17

 S
- Domenck S et al (2008) Influence of concentration and ionic strength on the adsorption kinetics of gelatin at the air/water interface. Colloids Surf A 331(1–2):48–55 Fu VF et al (2018) Effect of solium alginate on reverse floa-tion of hematite and its mechanism. Int J Miner Metall Mater 25:1113–1122 Shan J et al (2022) Characteristics of sodium alginate/antarc-
- Shan J et al (2022) Characteristics of sodium alginate/antarctic krill potentic composite fiber based on cellulose nanorystals modification: rheology, hydrogen bond, crystallization, strength, and water-resistance. Gels 8(3):139
 Shahin A, Joshi YM (2012) Physicochemical effects in aging aqueous Laponite suspensions. Langmuir 28(44):15674–15686
 Bonn D et al (1999) Laponite. What is the difference between a gel and a glass? Langmuir 15(2):73544–7358
 Zhang S et al (2008) Aqueous foams stabilized by Laponite and CTAB. Colloids Surf a 317(1–3):406–413
 Tomac A Amour I) Characterization of gelatin from the skin of most of the control of the cont

- 3(2):135-145

- Li Y-C, Schulz J, Grunlan JC (2009) Polyelectrolyte/nanosilicate thin-film assemblies: influence of pH on growth, mechanical behavior, and Tlammability. ACS Appl Mater Interfaces 1(10):2338–23047) Aqueous dispersions of silane-functionalized laponite clay platelets. A first step toward the elaboration of water-based polymer/clay nanocomposites. Langmuir 2005;1564–1571 tion of water-based polymer/clay nanocomposites. Langmuir 20(5):1564–1571 Kawabe S, Seki M, Tabata H (2014) Investigation of the sol-gel

- Kawaite S., Seci M., Tabata H (2014) Investigation of the sol-gel transition of gelanti using terahett time-domain spectroscopy. J. Appl Phys. https://doi.org/10.1063/14870954
 Derhach SR et al (2021) Rheological properties of fish gelatin modified with sodium alginate. Polymers 13(5):743
 Derhach SR et al (2015) The theology of gelatin hydrogets modified by scenarogena. J.WT-Food Sci Technol (361):612–639
 Derhach SR et al (2015) The theology of gelatin hydrogets modified by scenarogena J.WT-Food Sci Technol (361):612–639
 Section S. (1996) Unassual histotropic properties of species of sciences of Laponite RD. J. Colloid Interface Sci. 182(2):501–510
 Onnosa B. Labber C. Calbane R.O. (2008) Interaction of panometric
- 182(2):501–510
 Jonsson B, Labbez C, Cabane B (2008) Interaction of nanometric clay platelets. Langmuir 24(20):11406–11413
 Saunders JM et al (1999) A small-angle X-ray scattering study of the structure of aqueous Laponite dispersions. J Phys Chem B 103(43):9211–9218

- of the structure of aqueous Laponite dispersions. J Phys Chem B 103(43):211–9218

 98. Ma J et al (2014) Flow behavior, thixotropy and dynamical vis-coelasticity of sodium alginate aqueous solutions. Food Hydrocolloids 38:119–128

 90. Osorio FA et al (2007) Effects of concentration, bloom degree, and pH on gelatin melting and gelling temperatures using small amplitude oscillatory rheology. Int J Food Prop 10(4):841–851

 100. Johy-Duhamel C et al (2002) All gelatin networks: 2. The master curve for clasticity. Langmint 18(19):7188–71666

 101. Jatav S, Joshi YM (2014) Chemical stability of Laponite ous media. Appl Clay Sci 977:72–77

 102. Cai FF, Heid S, Boccaccini AR (2021) Potential of Laponite® incorporated oxidized alginate—gelatin (ADA-GEL) composite hydrogels for extrusion-based 3D printing. J Biomed Mater Res B Appl Biomater 109(8):1000–1104

 103. Nair SH et al (2007) Swelling and mechanical behavior of modified poly (vinyal achosh/Japonite annocomposite membranes. J
- Nasi Sri et at (20/7) Swelting and incrimate intervative to mout-fied poly (vinyl alcoholyllaponite nanocomposite membranes, J Appl Polym Sci 103(5):2896–2903
 Qiao C, Cao X, Wang F (2012) Swelling behavior study of physically crosslinked gelatin hydrogels. Polym Polym Compos 20(1–2):53–58
- 20(1-2)x53-58
 105. Zhang Y et al (2015) In vitro study of directly bioprinted perfusable vasculature conduits. Biomater Sci 3(1):134-143
 106. Knežević D, Savić V (2006) Mathematical modeling of changing of dynamic viscosity, as a function of temperature and pressure, of mineral oils for hydraulic systems. Facta Univ Ser Mech Eng 4(1):27:24
- of minetar one way a system of the free distribution of the free distri

- methacryloyl (MC/GeIMA) bionik with high shape integrity.
 ACS Appl Bio Mater 3(3):1815-1826
 109. Tan JJY, Lee CP, Hashimoto M (2020) Preheating of gelatin improves its primability with transglutaminase in direct link writing 3D printing. Int J Bioprint 6(4):296
 110. Nishinari K et al (1997) Gel-ole transition of methylcellulose. Macromol Chem Phys 198(4):1217-1226
 111. Wilson SAS et al (2017) Shae-thinning and thermo-reversible nanoengineered his for 3D bioprinting. ACS Appl Mater Interfaces 9(50):43449-4348
- Liu W et al (2017) Extrusion bioprinting of shear-thinning gelatin methacryloy) bioinks. Adv Healthcare Mater 6(12):1601451
 Pan J et al (2016) Effect of temperature on grease flow properties in pipes. Tribol Trans 59(3):569–578



Progress in Additive Manufacturing

- Poslinski A et al (1988) Rheological behavior of filled poly-meric systems I. Yield stress and shear-thinning effects. J Rheol

- 114. Poslinski A et al (1990) Subsequent in Miller Stephen Ste 119. Xu HH et al (2017) Calcium phosphate cements for bone engi-
- neering and their biological properties. Bone research 5(1):1–19

 120. John J et al (2017) Rheology of solid-like ethanol fuel for hybrid rockets: Effect of type and concentration of gellants. Fuel
- 209-96-108

 121. Qin Jet al (2019) Tailor the rheological properties of silver front side metallization paste for crystalline silicon solar cells. Mater Sci Forum 956:12-20

 122. Jin Zet al (2021) Monitoring anomalies in 3D bioprinting with deep neural networks. ACS Biomater Sci Eng. https://doi.org/10.
- Nig H, Zhou T, Joo SW (2023) Machine learning boosts three-dimensional bioprinting. Int J Bioprint 9(4):739
 Shin J et al (2022) Optimized 3D bioprinting technology based on machine learning: a review of recent trends and advances. Micromachines 13(3):360
- 125. Yu C, Jiang J (2020) A perspective on using machine learning in 3D bioprinting. Int J Bioprint 6(1):253
 126. Freeman S et al (2022) Bioink formulation and machine learning-empowered bioprinting optimization. Front Bioeng Biotechnol 16(4):253
- 10:913579

 127. Dong H et al (2023) Robotic-assisted automated in situ bioprint-
- ing. Int J Bioprint 9(1):629

 128. Sun J et al (2023) Machine learning and 3D bioprinting. Int J Bioprint 9(4):717
- Sun J et al (2022) Machine learning applications in scaffold based bioprinting. Mater Today Proc 70:17–23
 Shi J et al (2019) Multi-objective optimization design through machine learning for drop-on-demand bioprinting. Engineering 5(3):586–593

- Goh GD, Sing SL, Yeong WY (2021) A review on machine learning in 3D printing: applications, potential, and challenges. Act of the Rev 54(1):63. Per section 132. Nuclemental A. Groll J (2022) Machine learning reveals a general understanding of printability in formulations based on rheology additives. Adv Sc 9 (29):2202638.
 Nuclemental A. Groll J (2021) Machine learning to explain printability induced by rheology additives. Adv Sc https://doi.org/10.1007/advs.2022.0368
 Lee J et al (2020) Machine learning-based design strategy for 3D printable biolist: Falsier modulus and visid stress determine.
- Lee J et al. (2020) maturine tealming-oased usergin stategy into 3D printablib, bionix: classic modulus and yield stress determine printablity. Biofabrication 12(3):035018
 Nocheseda CUC et al. (2021) 3D printing of metals using biode-gradable cellulose hydrogel inks. Addit Manuf 48:102380
 Challagulla NV et al. (2020) Recent developments of nanomate-tion.
- Challagulla NV et al. (2020) Recent developments of nanomaterial applications in additive manufacturing: a brief review. Curr Opin Chem Eng 28:75–82
 Holness FB, Price AD (2017) Direct link writing of 3D conductive polyaniline structures and rheological modelling. Smart Mater Struct 27(1):10500
 Sun J et al. (2018) Extrusion-based food printing for digitalized food definitioned meeting control at Long Eng. 27(2):113
- food design and nutrition control. J Food Eng 220:1–11

 139. Elbadawi M et al (2020) 3D printing tablets: Predicting printability and drug dissolution from rheological data. Int J Pharm
- ability and drug dissolution from rheological data. Int J Pharm 500:11986.

 140. Yu H-Y, Ma D-D, Wu B-L (2017) Gelatin/alginate hydrogel scaffolds prepared by 3D bioprinting promotes cell adhesion and proliferation of human dental pulp cells in vitro. J South Med Univ 375/668-672

 141. Sarker B et al (2014) Evaluation of fibroblasts adhesion and proliferation on alginate-gelatin crosslinked hydrogel. PLoS ONE 9(9):e107952

Springer Nature or its licensor (e.g. a society or other partner) holds exclusive rights to this article under a publishing agreement with the author(s) or other rightsholder(s); author self-archiving of the accepted manuscript version of this article is solely governed by the terms of such publishing agreement and applicable law.

Authors and Affiliations

Imtiaz Qavi¹ · Sampa Halder¹ · George Tan¹

☑ George Tan george.z.tan@ttu.edu

Department of Industrial, Manufacturing, and Systems Engineering, Texas Tech University, 905 Canton Ave, Lubbock, TX 79409, USA